Ore Geology Reviews 89 (2017) 228–252

Contents lists available at ScienceDirect

Ore Geology Reviews

journal homepage: www.elsevier.com/locate/oregeo

# Delineation of potential exploration targets based on 3D geological modeling: A case study from the Laoangou Pb-Zn-Ag polymetallic ore deposit, China

Fan Yang [a], Gongwen Wang [a,*], M. Santosh [a,b,*], Ruixi Li [a], Li Tang [a], Huawen Cao [c], Nana Guo [d], Chao Liu [e]

[a] School of Earth Sciences and Resources, China University of Geosciences Beijing, 29 Xueyuan Road, Beijing 100083, China
[b] Department of Earth Sciences, University of Adelaide, SA 5005, Australia
[c] Chengdu Center, China Geological Survey, Chengdu 610081, China
[d] Luanchuan Burcan of Geology and Resources, Luoyang 417500, China
[e] Shandong Lunan Geology and Exploration Institute, Jining 272100, China

ARTICLE INFO

*Article history:*
Received 29 September 2016
Received in revised form 22 May 2017
Accepted 9 June 2017
Available online 17 June 2017

*Keywords:*
3D geological modeling
Mineral potential targets
3D weight of evidences
Fractal analysis
Laoangou ore deposit

ABSTRACT

The Laoangou Pb-Zn-Ag polymetallic ore deposit (LAG) is a hydrothermal vein-type deposit in the East Qinling polymetallic metallogenic belt, which is controlled by NW-, NE- and nearly SN-trending faults and mainly hosted in the dolomite marble of Meiyaogou and Baishugou formations within the Luanchuan ore district (LOD). Although district-scale metallogenic prediction related to the Pb-Zn-Ag deposits in the LOD has been attempted, there have been no studies to formulate a detailed deposit-scale metallogenic prediction of the Pb-Zn-Ag deposit in 3D space. Here we selected the LAG to formulate a metallogenic prediction model for Pb-Zn-Ag deposit based on data from 1:10,000 scale geological map, and 66 boreholes and 39 sections of exploration lines on 1:1000 scale, to extract the salient spatial features of the deposit. We apply ordinary weights and weighted weights of evidence, followed by boosted weights of evidence, logistic regression and information entropy for integrating the features of the ore deposit for exploration targeting. The C–V fractal method is applied to classify the probabilities. Accordingly, three levels of exploration targets are delineated: the first level targets are mainly distributed in the periphery of known orebodies (M2, M3, II-3 and VI), which are also located in the ore-controlling strata and fault zones; the second level targets are located in the region of known orebodies, indirectly confirming that the prediction result is reliable; and the third level targets, which are mainly located at the contact between ore-controlling strata and metagabbro bodies, offer new targets for exploration in this ore district. Combining our results obtained in this study with those in previous studies, we provide some guidelines for exploration targets in the Pb-Zn-Ag deposits in the LOD, which might help in more effectively delineating the target zones.



## 1. Introduction

The depletion of shallow ore resources has warranted deep exploration and prediction of prospecting potential targets. The 3D geological modeling method, which mainly utilizes detailed geological maps, geologic survey records, structural information, and geophysical and geochemical data to construct the 3D geological images of strata, structure, rock formation and ore body, geophysical anomaly and geochemical anomaly, has become an important tool for deep prospecting work (Kaumfmann and Martin, 2008; Wang and Huang, 2012). Such 3D geological models help to better understand geological structure spatial relationship, aiding in identifying exploration and prospecting targets (Wang et al., 2015; Mejía-Herrera et al., 2015). Furthermore, 3D geological models can also be employed to evaluate the genetic aspects through spatial analysis or logical calculation associated with regional metallogenic concepts and typical ore deposit models (Pouliot et al., 2008; Wang and Huang, 2012). Currently, 3D geological modeling technique is used widely to analyze geological formations enriched in resources and their spatial distribution (Shao et al., 2011). Special softwares (e.g. Micromine, Gocad, Surpac and 3Dmine) help in data processing and construction of complex 3D models. Although the use of geological maps, and field and

* Corresponding authors at: School of Earth Sciences and Resources, China University of Geosciences Beijing, 29 Xueyuan Road, Beijing 100083, China (M. Santosh).
*E-mail address:* gwwang@cugb.edu.cn (G. Wang).

http://dx.doi.org/10.1016/j.oregeorev.2017.06.013
0169-1368/

structural information to build precise 3D models remain as a challenge (Kaufmann and Martin, 2008), the models allow to better integrate several features and to understand their implications (Martelet et al., 2004; Wang et al., 2015; Li et al., 2016). One of the challenges in the application of these data and techniques is the quantitative extraction of useful exploration criteria from 3D datasets and effectively integrate all of the available 3D information to guide future deep exploration (Mao et al., 2011b; Yuan et al., 2014; Li et al., 2015a).

Mineral potential targets based on 3D geological modeling, which is an effective method of target identification during mineral exploration (Agterberg et al., 1990; Bonham-Carter, 1994; Wang et al., 2011b; He et al., 2013; Shahriari et al., 2013; Luz et al., 2014), aim to delineate potential target zones and estimate the probable size of undiscovered ore deposits as well as to estimate the total mineral resource of certain types of mineral deposits (Singer, 2008; Carranza, 2009; Carranza and Sadeghi, 2010; Wang et al., 2012a, 2012b, 2017; Li et al., 2015a; Wang et al.,

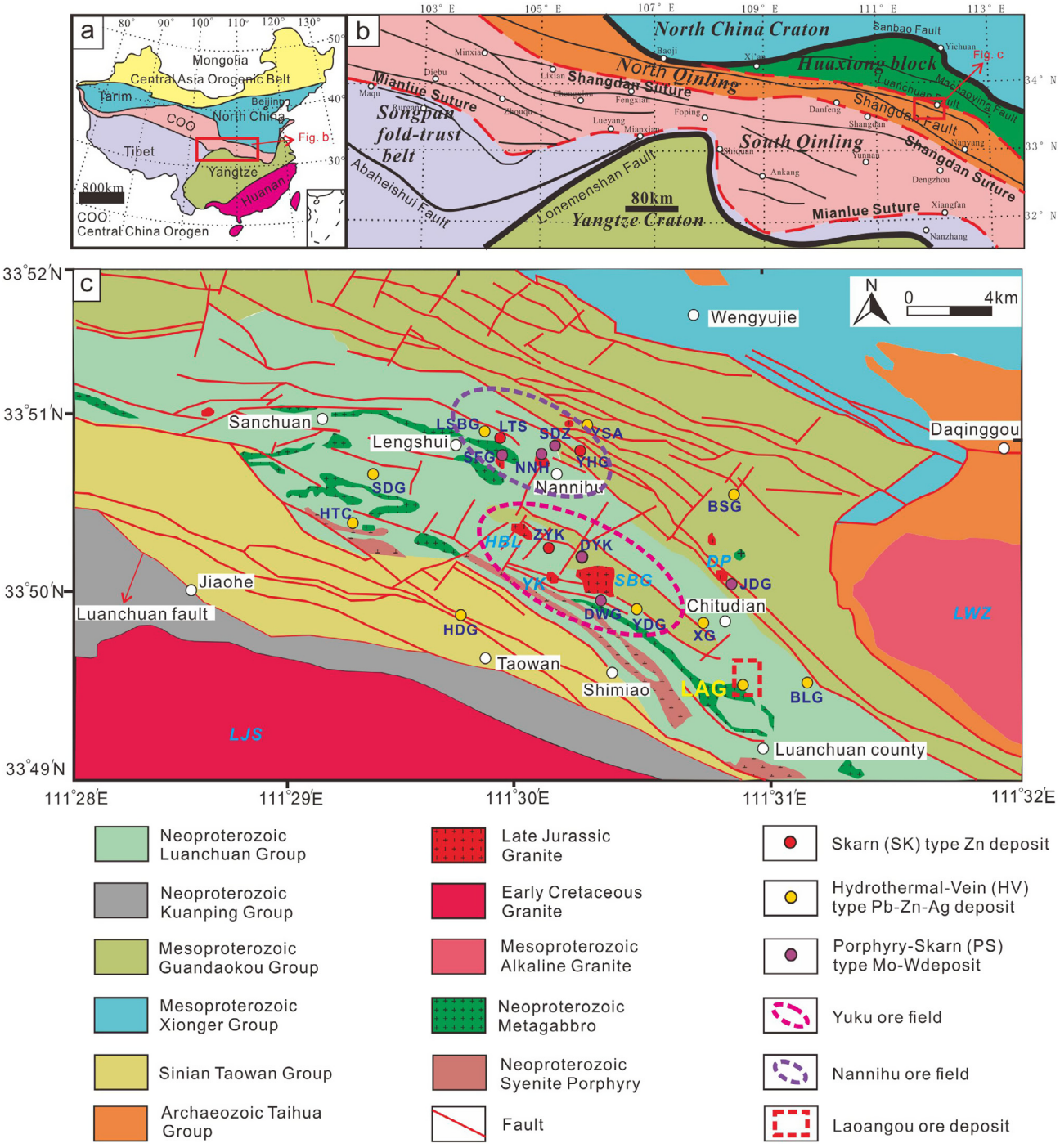


**Fig. 1.** (a) Tectonic map of China, showing the location of the Central China orogenic belt. (b) Tectonic subdivision of the Qinling Orogen, showing the location of the LOD. (c) Geology and mineral resource of the LOD, showing the spatial distribution with known ore occurrences and the location of the LAG (Modified after Duan et al., 2010; Cao et al., 2015; Yang et al., 2016). Abbreviations of deposits: BLG, Bailugou; DWG, Dawanggou; DYK, Dongyuku; HDG, Hongdonggou; HTC, Hetaocha; JDG, Jiudinggou; LSBG, Lengshuibeigou; LTS, Luotuoshan; NNH, Nannihu; SDZ, Sandaozhuang; SFG, Shangfanggou; XG, Xigou; YDG, Yindonggou; YHG, Yinhegou; YSA, Yangshuao; ZYK, Zhongyuku; LAG, Laoangou. Abbreviations of granites: DP, Daping; HBL, Huangbeiling; SBG, Shibaogou; YK, Yuku; LJS, Laojunshan; LWZ, Longwangzhuang.

2017). Based on 3D modeling and application of statistical methods such as weights of evidence, logistic regression, information entropy and fractal analyses, potential target zones for prospecting have been successfully identified in some recent studies (Hamedani et al., 2012; Li et al., 2015a; Wang et al., 2015, 2017; Li et al., 2016). The method of weights of evidence based on Bayes' rule has been used for 2D data integration and modeling (Agterberg, 2011; Mohammady et al., 2012; Ozdemir and Altural, 2013; Nielsen et al., 2015; Ford et al., 2016). Through these methods, spatial relationships between data inputs and mineralization have also been quantified (Yuan et al., 2014). The degree of correlation between a particular condition or pattern and a set of data points representing known ore deposits or occurrences derived through these techniques also help to identify the favorable zones for mineral exploration (Agterberg et al., 1990; Cheng and Agterberg, 1999; Yuan et al., 2014). Several recent studies have used the weights of evidence for conducting the 3D potential exploration targets (Yuan et al., 2014; Li et al., 2016; Wang et al., 2015, 2017).

The Laoangou Pb-Zn-Ag polymetallic ore deposit (LAG) in southeastern part of the Luanchuan polymetallic ore district (LOD) is located at the margin of the North China Craton within the east Qinling orogenic belt (Cao et al., 2015; Li et al., 2015b; Yang et al., 2016) (Fig. 2b). Mineralization in this hydrothermal-vein deposit is controlled by NW- and NE-trending faults (Yang et al., 2016). Although previous 3D geological modeling (Zhu, 2013; Wang et al., 2011a) and 3D metallogenic prediction (Wang et al., 2011a, 2015) have been attempted in the LOD, several aspects remain unresolved. Previous work mainly focused on the district-scale metallogenic prediction of Mo and Pb-Zn-Ag deposits in the LOD (Wang et al., 2015; Yang, 2016), whereas that for deposit-scale Pb-Zn-Ag mineral has not been performed systematically. The currently available models for ore strata, structure and host rock of the LOD are based on limited data, and are therefore nor precise and require further optimization. Also 3D geological models of the LAG, which is one of the hydrothermal vein-type deposits in the LOD, have not been attempted as yet, with no reliable information on the deep structure for metallogenic prediction of Pb-Zn-Ag mineral.

In this study, we attempt a systematic reconstruction of the 3D geological models (orebody, strata, fault and host metagabbro body) based on the data obtained from geological maps, cross-sections and boreholes which provides insights into the regional geology and processes of ore-formation. We use the following information to formulate the models: (1) 1:10,000 scale geological map and two sections; (2) corresponding fault lines from the map; and (3) data from 66 boreholes and 39 sections of prospecting lines. Ultimately, a comprehensive deposit-scale 3D mineral potential targeting model was formulated to delineate the subsurface mineral exploration potential in the LAG. We then employ weights of evidence, logistic regression, information entropy and fractal methods to analyze and integrate geological information and exploration criteria. The potential targets delineated in this study are expected to contribute to further guide the deep prospecting work of the LAG.

## 2. Geological background

### 2.1. Regional geological and tectonic framework

The Central China orogenic belt (COO), located in the southern margin of the North China Craton to the north of Yangtze Craton, extends from West Kunlun in the west to Sulu in the east (Bao et al., 2014; Cao et al., 2015), is composed of the Qilian, West Qinling, East Qinling and Dabie orogens, stretching over 4000 km (Pirajno, 2013; Bao et al., 2014; Dong and Santosh, 2016; Hu et al., 2016; Deng et al., 2016) (Fig. 1a, b). The CCO witnessed opening and closure of paleo-oceans between terranes, and subsequent collision and suturing between the North China Craton and Yangtze Craton during the Triassic (Meng and Zhang, 2000; Sun et al., 2002; Li et al., 2015; Tang et al., 2016; Dong and Santosh, 2016; Yang et al., 2017), preserving the records of Late Mesoproterozoic to Cenozoic tectonics (Ratschbacher et al., 2003; Bao et al., 2014; Cao et al., 2015; Xue et al., 2017). Among these, the Qingling orogen which extends approximately 1000 km from west to east and is bounded by the Sanbao fault to the north and the Longmenshan-Dabashan fault to the south (Fig. 1b) contains four terranes, including the southern margin of the North China Craton, North Qinling Terrane, South Qinling Terrane, and the northern margin of the Yangtze Craton from north to south (Bao et al., 2014; Xiao et al., 2017; Dong and Santosh, 2016). From north to south, the North China Craton and the North Qinling Terrane are separated by the Luanchuan fault (Bao et al., 2014), the North Qinling Terrane and the South Qinling Terrane by the Shangdan fault (Li et al., 2015b), and the South Qinling Terrane and the Yangtze Craton by the Mianlue fault (Dong et al., 2011; Wang et al., 2013; Wu and Zheng, 2013) (Fig. 1b).

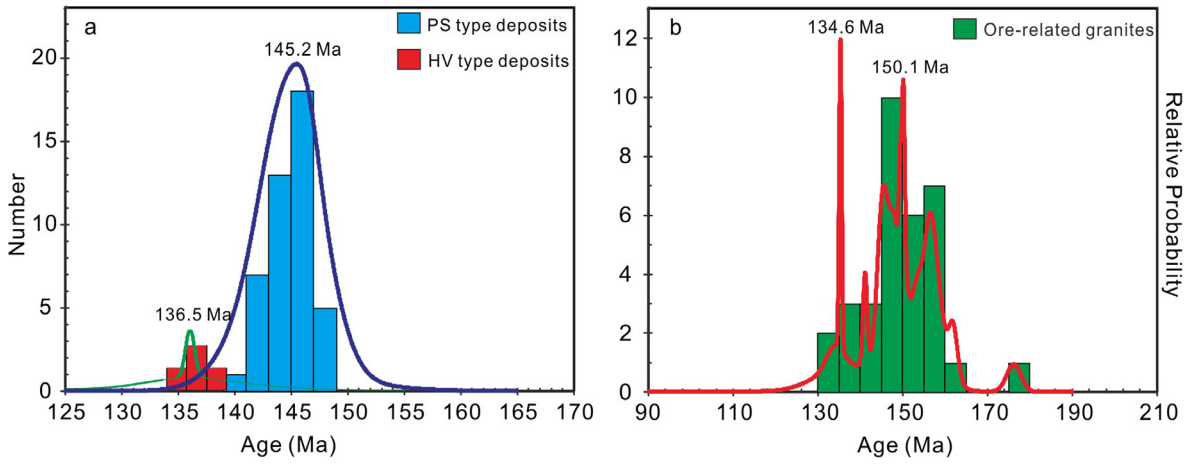


**Fig. 2.** Age data histograms and probability curves, (a) compilation of data on porphyry-skarn (PS) type Mo-W deposits and hydrothermal-vein (HV) type Pb-Zn-Ag deposits in the LOD; (b) compilation of data on ore-related granites in the LOD. Data sources: Mao et al. (2005, 2010), Bao et al. (2014), Li et al. (2015), Yang et al. (2016), Xue et al. (2017) and references therein.

The East Qingling metallogenic belt, comprising the Huaxiong Terrane which is located the southern margin of the North China Craton and the North Qinling Terrane Paleozoic accretionary Terrane at the northern margin of the Qingling region (Mao et al., 2011a; Chen and Santosh, 2014; Bao et al., 2014; Cao et al., 2015; Tang et al., 2015; Dong and Santosh, 2016), preserves the signature of an active continental margin associated with the subduction-collision history between the North China Craton and the Yangtze Craton during the Triassic (Li et al., 2005, 2012, 2015c; Dong and Santosh, 2016; Xue et al., 2017; Yang et al., 2017). From the southern margin of the North China Craton to the northern margin of the Qingling region, the Huaxiong Terrane and the North Qinling Terrane Paleozoic accretionary Terrane are separated by the Sanbao fault, the Luanchuan fault and Shangdan fault, respectively (Fig. 1b). The LOD which is located at the southern margin of the Huaxiong Terrane near the Luanchuan fault that forms the southern boundary fault of the North China Craton (Cao et al., 2015) (Fig. 1b).

### 2.2. Geological background within the LOD

The dominant rocks exposed in the LOD, including the Mesoproterozoic Guandaokou, Neoproterozoic Luanchuan, Sinian Taowan and Neoproterozoic Kuanping groups from top to bottom (Fig. 1c), comprise Proterozoic and Paleozoic rocks (Yang et al., 2016). The Mesoproterozoic Guandaokou and Neoproterozoic Luanchuan groups consisting of a suite of carbonaceous carbonate-shale-chert sequence form the main host strata of Mo-Pb-Zn polymetallic ores. The Guandaokou group is unconformably overlain by the Luanchuan group (Yang et al., 2016). The Sinian Taowan group contains carbonatites metamorphic siltstone, quartzite, phyllite, conglomerate and argillaceous marble, which unconformably overlie the Luanchuan group (Yang et al., 2016). The Neoproterozoic Kuanping Group, including a succession of metamorphic clastic and mafic igneous rocks and carbonatites located in the south (Duan et al., 2010; Li et al., 2012), which unconformably overlie the Luanchuan group (Tang et al., 2016; Yang et al., 2016) (Fig. 1c).

The faults and folds developed in the LOD mainly include the Luanchuan fault and its branches, which are mainly NE- and NW-trending and record multi-stage brittle- and ductile-deformation associated with the Triassic continental collision between the North China Craton and the Yangtze Craton (Cao et al., 2015; Yang et al., 2016, 2017) (Fig. 1c). The regional structures mainly include the WNW-striking thrust faults, subordinate NE-striking strike-slip faults as well as WNW-trending interlayer fractures developed in the Luanchuan and Guandaokou groups (Yang et al., 2016), which are the main ore-controlling structures of the Mo-Pb-Zn polymetallic deposits (Cao et al., 2015; Li et al., 2015b; Yang et al., 2016).

The major intrusions in the LOD are Neoproterozoic metagabbro dykes, late Jurassic – early Cretaceous granites, Mesoproterozoic alkaline granites and Neoproterozoic syenite porphyries (Fig. 1c). The ca. 830 Ma metagabbro dykes mainly occur in the Luanchuan group, and show a close relationship with rifting along the southern margin of the North China Craton associated with the breakup of the Rodinia supercontinent (Wang et al., 2011a). The granitoids exposed in LOD mainly include the late Jurassic granites, early Cretaceous granites, Mesoproterozoic alkaline granites and Neoproterozoic syenite porphyries, which are distributed in the Laojunshan, Shibaogou and Longwangzhuang regions of the LOD (Fig. 1c). The intrusions show NW and NNE trend and occur along the tectonic intersection area showing close relationship with mineralization (Yang et al., 2016) (Fig. 1c). Among these intrusions, the late Jurassic-early Cretaceous granites make up the most major intrusion. Which are characterized by the I-type granites (Li et al., 2012, 2015b; Bao et al., 2014; Zhang, 2014; Cao et al., 2015), and considered the magma source from the lower crust with involvement of the upper mantle associated with the large-scale lithospheric thinning beneath the North China Craton during the Mesozoic (Li et al., 2013; Santosh, 2013; Zhai and Santosh, 2013; Zhu et al., 2009; Yang et al., 2017).

### 2.3. Mineralization within the LOD

The LOD which is located in the core of a molybdenum-bearing polymetallic ore belt in the East Qinling metallogenic belt includes the famous Nannihu and Yuku ore fields (Mao et al., 2008, 2011; Li et al., 2012) (Fig. 1c), shows a regular spatial distribution of the different deposits in the two ore fields (Cao et al., 2015). The two ore fields (Nannihu and Yuku ore fields) are characterized by similar metallogenic systems, with three types of deposits including the proximal porphyry-skarn (PS) type Mo-W deposits, intermediate skarn (SK) type Zn deposits and distal hydrothermal-vein (HV) type Pb-Zn-Ag deposits from the center to the periphery in each ore field (Wang et al., 2013; Cao et al., 2015; Yang et al., 2016) (Fig. 1c). The proximal PS type Mo-W deposits mainly including the Nannihu, Sandaozhuang and Shangfanggou deposits of Nannihu ore field, as well as Dongyuku and Dawanggou deposits of Yuku ore field are distributed at the inner and outer contact zones between the porphyry and the hornfels and subordinately in the skarn and marble, and are characterized by typically zoned hydrothermal alterations from the porphyry to the wall rocks (Yang et al., 2013; Cao et al., 2015) (Fig. 1c). The intermediate SK type Zn deposits are mainly represented by the Luotuoshan and Yinhegou deposits of Nannihu ore field and the Zhongyuku deposit of Yuku ore field which are mostly located within the contact zones between the intrusions and the carbonate sedimentary rocks (Fig. 1c). They are characterized by extensive wall rock alteration around the orebodies (Cao et al., 2015). The distal HV type Pb-Zn-Ag deposits include these typical Lengshuibeigou, Sandaogou and Hongdonggou deposits of the Nannihu ore field, as well as the Bailugou, Xigou, Yindonggou and Laoangou deposits of the Yuku ore field, and are structurally-controlled by the NE-trending strike-slip and the NWW-trending bedding faults as well as WNW-trending interlayer fractures and folds at the periphery of the two ore fields (Cao et al., 2015; Yang et al., 2016) (Fig. 1c). Moreover, the distal HV type Pb-Zn-Ag deposits occur as veins and are spatially hosted within mineralized fault zones, interlayer fractures and fold zones.

### 2.4. Geodynamic setting

Li et al. (2012) proposed that ore-bearing plutons possess the features of post-collisional intrusions, and proposed that magmatism in the post-collisional setting in the Luanchuan ore belt commenced at 157 Ma, with a peak at ~145 Ma and lasted until ~115 Ma (Li et al., 2012). In the compiled age data from the LOD shown in Fig. 2, the HV type Pb-Zn-Ag deposits show age peaks at 136.5 Ma (Fig. 2a), the PS type Mo-W deposits display age peaks at 145.2 Ma (Fig. 2a), and the ore-bearing granites exhibit age peaks from 134.6 Ma to 150.1 Ma (Fig. 2b) (Table 1). These ages are broadly common throughout the metallogenic belt in the LOD and are consistent with the results proposed by Li et al. (2012). From the available age data (Li et al., 2012; Cao et al., 2015; Yang et al., 2016; Xue et al., 2017), the collision between the North China Craton and the Yangtze Craton (Qinling orogen) began in the Triassic (Zhang et al., 2001; Guo et al., 2005) and continued to the late Triassic (~211 Ma) (Jiang et al., 2010). The Qinling orogen then evolved into the intra-continental orogenic stage with thrusting and uplift caused by continental collision and extension (Zhang et al., 2001; Liu et al., 2004; Jiang et al.,

**Table 1**
Isotopic ages reported from granitic plutons, deposits of porphyry-skarn Mo-W deposit, hydrothermal-vein Pb-Zn deposit and skarn Pb-Zn deposit in the LOD.

| Deposits/granites | Sample Types | Methods | Age (Ma) | Reference |
|---|---|---|---|---|
| *Porphyry-skarn Mo-W deposit* | | | | |
| Nannihu | Molybdenite | Re–Os | 143.9 ± 2.1 | Xiang et al. (2012) |
| | Molybdenite | Re–Os | 144.4 ± 2.2 | |
| | Molybdenite | Re–Os | 145.8 ± 2.3 | |
| | Molybdenite | Re–Os | 145.8 ± 2.2 | |
| | Molybdenite | Re–Os | 143.4 ± 2.0 | |
| | Molybdenite | Re–Os | 139.3 ± 2.3 | Mao et al. (2008) |
| | Molybdenite | Re–Os | 144.8 ± 2.1 | Li et al. (2004) |
| Sandaozhuang | Molybdenite | Re–Os | 145 ± 2.2 | Li et al. (2004) |
| | Molybdenite | Re–Os | 143.5 ± 2.9 | Mao et al. (2008) |
| | Molybdenite | Re–Os | 144.2 ± 1.5 | |
| | Molybdenite | Re–Os | 143.8 ± 1.8 | |
| | Molybdenite | Re–Os | 144.6 ± 2.5 | Xiang et al. (2012) |
| | Molybdenite | Re–Os | 146.5 ± 2.3 | |
| | Molybdenite | Re–Os | 146.0 ± 2.3 | |
| | Molybdenite | Re–Os | 144.5 ± 2.3 | |
| | Molybdenite | Re–Os | 146.0 ± 2.2 | |
| Shangfanggou | Molybdenite | Re–Os | 144.8 ± 2.1 | Li et al. (2004) |
| | Molybdenite | Re–Os | 142.9 ± 1.6 | Mao et al. (2008) |
| | Molybdenite | Re–Os | 141.8 ± 3.6 | |
| Yuku | Molybdenite | Re–Os | 146.9 ± 2.1 | Li et al. (2015b) |
| | Molybdenite | Re–Os | 145.9 ± 2.1 | |
| | Molybdenite | Re–Os | 147.1 ± 2.1 | |
| | Molybdenite | Re–Os | 146.3 ± 2.2 | |
| | Molybdenite | Re–Os | 146.7 ± 2.2 | |
| | Molybdenite | Re–Os | 144.6 ± 2.2 | |
| Majuan | Molybdenite | Re–Os | 141.8 ± 2.1 | Li et al. (2007) |
| Dongyuku | Molybdenite | Re–Os | 146.6 ± 0.9 | Zhang (2014) |
| Jiudinggou | Molybdenite | Re–Os | 141 ± 2.5 | |
| Dawanggou | Molybdenite | Re–Os | 147.3 ± 2.5 | Mao et al. (2008) |
| | Molybdenite | Re–Os | 146.8 ± 2.3 | |
| | Molybdenite | Re–Os | 147.5 ± 2.2 | |
| | Molybdenite | Re–Os | 147.5 ± 2.1 | |
| | Molybdenite | Re–Os | 142.9 ± 1.9 | |
| | Molybdenite | Re–Os | 141.5 ± 2.0 | |
| *Hydrothermal-vein Pb-Zn-Ag deposit* | | | | |
| Lengshuibeigou | Quartz | Ar–Ar | 136.1 ± 0.4 | Wang et al. (2013) |
| Sandaogou | Sphalerite | Rb–Sr | 137.3 ± 5.4 | Cao et al. (2015) |
| Xigou | Sphalerite | Rb–Sr | 137.7 ± 5.7 | |
| Hongdonggou | Sphalerite | Rb–Sr | 135.7 ± 3.2 | Yang et al. (2016) |
| *Skarn type Pb-Zn deposits* | | | | |
| Luotuoshan | Sphalerite, Galena and Pyrite | Rb–Sr | 137.3 ± 2.6 | Yang et al. (2015) |
| *Ore-related granites* | | | | |
| Nannihu | Granite porphyry | LA-ICP-MS U–Pb | 146.7 ± 1.2 | Xiang et al. (2012) |
| | Granite porphyry | LA-ICP-MS U–Pb | 145.2 ± 1.5 | |
| | Granite porphyry | LA-ICP-MS U–Pb | 176.3 ± 1.7 | |
| | Granite porphyryn | LA-ICP-MS U–Pb | 158.2 ± 1.2 | |
| | Granite porphyry | LA-ICP-MS U–Pb | 145.7 ± 1.2 | |
| | Porphyritic granite | LA-ICP-MS U–Pb | 149.6 ± 0.4 | Bao et al. (2014) |
| | Granite porphyry | SHRIMP U–Pb | 157 ± 3 | Mao et al. (2010) |
| | Porphyritic granite | SHRIMP U–Pb | 158.2 ± 3.1 | Mao et al. (2005) |
| Shangfanggou | Granite porphyry | LA-ICP-MS U–Pb | 135.4 ± 0.3 | Bao et al. (2014) |
| | Granite porphyry | SHRIMP U–Pb | 158 ± 3 | Mao et al. (2010) |
| | Porphyritic granite | SHRIMP U–Pb | 157.6 ± 2.7 | Mao et al. (2005) |
| | Granite porphyry | LA-ICP-MS U–Pb | 135.4 ± 0.3 | Bao et al. (2009) |
| | Porphyritic granite | LA-ICP-MS U–Pb | 153.2 ± 1.3 | Li et al. (2015b) |
| Shibaogou | Monzonite granite | LA-ICP-MS U–Pb | 156 ± 1 | Yang et al. (2012) |
| | Monzonite granite | LA-ICP-MS U–Pb | 157 ± 1 | |
| | Monzonite granite | SHRIMP U–Pb | 147.2 ± 1.7 | Bao et al. (2014) |
| | Syenogranite porphyry | SHRIMP U–Pb | 145.3 ± 1.4 | |
| | Monzonite granite | SHRIMP U–Pb | 150.3 ± 1.5 | Liu (2007) |
| Yuku | Granite porphyry | LA-ICP-MS U–Pb | 150.5 ± 0.8 | Zhang (2014) |
| | Granite porphyry | LA-ICP-MS U–Pb | 154.1 ± 1.8 | |
| | Granite porphyry | LA-ICP-MS U–Pb | 148.3 ± 1 | |
| | Granite porphyry | LA-ICP-MS U–Pb | 154.1 ± 1.8 | Li et al. (2015b) |
| | Granite porphyry | LA-ICP-MS U–Pb | 148.3 ± 1.0 | |
| | Granite | LA-ICP-MS U–Pb | 149.6 ± 2.4 | Xue et al. (2017) |
| Daping | Granite porphyry | LA-ICP-MS U–Pb | 141.2 ± 0.5 | Zhang (2014) |

2010). Subsequently, magmas intruded as small-scale stocks, dikes, and pipes in the Jurassic, and intrusions formed large-scale stocks and batholiths in the Cretaceous (Liu, 2007; Li et al., 2012).

## 3. Deposit geology

### 3.1. Stratigraphy and intrusions

The LAG is located in the southeastern part of Chitudian Pb-Zn-Ag polymetallic metallogenic belt of the LOD, and classified as the hydrothermal-vein (HV) type Pb-Zn-Ag deposits controlled by NW-, NE- and nearly SN-trending faults in the LOD (Guang et al., 2013; Yang et al., 2016) (Fig. 1c). Regionally, the exposed strata in the LAG include those belonging to the Dahongkou, Meiyaogou, Nannihu, Sanchuan formations of the Luanchuan group and Baishugou formation of the Guandaokou group, together with Proterozoic and Paleozoic units (Fig. 3a, b). The Dahongkou formation is composed of biotite trachyte, sericite-albite schist and dolomite marble, the Meiyaogou formation contains dolomite marble, sericite-quartz schist, biotite schist and carbonaceous slate, the Nannihu formation includes quartz marble, biotite marble, sericite-quartz schist and metasiltstone, and the Sanchuan formation contains biotite marble and metasiltstone, and Baishugou formation includes biotite marble, sericite-quartz schist and carbonaceous slate specifically (Fig. 3a, b). Among these formations, the Meiyaogou and Baishugou formations are the major ore-bearing strata (Fig. 3a, b), and host rocks mainly include banded dolomite marble, sericite-quartz schist, biotite schist and

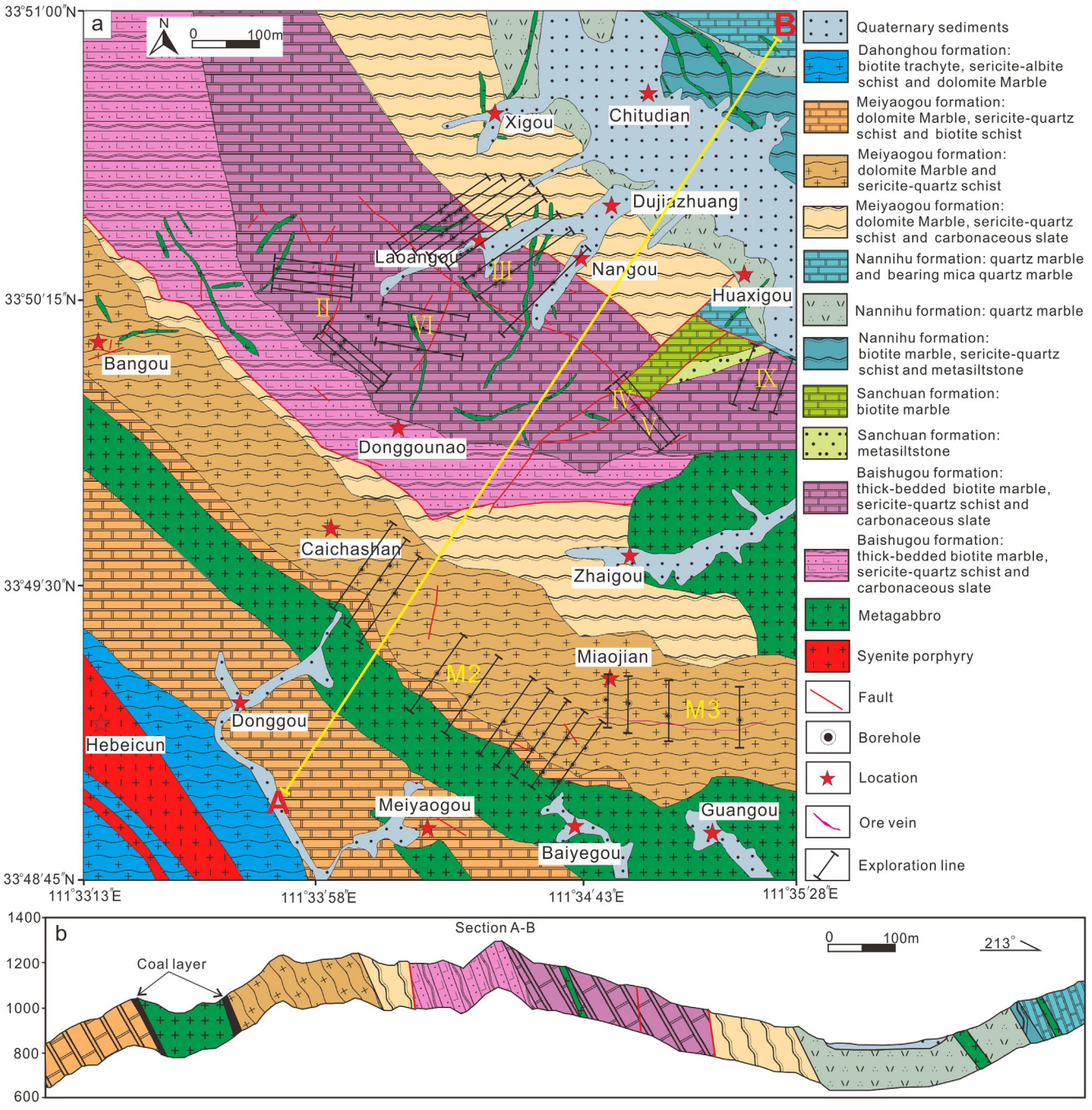


**Fig. 3.** Geology and mineral resource of the LAG, showing the spatial distribution with known orebodies and exploration lines (Modified after Guang et al., 2013).

carbonaceous slate of Meiyaogou formation and thick-bedded biotite marble, sericite-quartz schist and carbonaceous slate of Baishugou formation. A number of faults have been recognized surrounding the deposit, and they include three types with NWW-NW, NNE, and NE-NEE trends which form the branches of the Luanchuan fault (Cao et al., 2015; Yang et al., 2016) (Fig. 3a, b).

The intrusive suite in the LAG mainly includes metamorphosed gabbro dykes and syenite porphyries (Fig. 3a, b). The metamorphosed gabbro dykes are mainly distributed in the southwestern part of the LAG, and intruded into the Baishugou, Nannihu and Meiyaogou formations. The gabbro is grayish green colored, fine to medium grained and typical gabbroic texture, including the minerals of amphibole (40–55 vol.%), plagioclase (30–50 vol.%) and biotite (3–10 vol.%), with apatite, pyrite, magnetite and titanite as accessory. The gabbro dykes mostly occur at the periphery of the known orebodies (Fig. 3a, b), suggesting a close spatial relationship with the mineralization and serving as a guide for prospecting (Yang et al., 2016). The syenite porphyries are located in the southwestern segment of the LAG, and away from the orebodies indirectly suggesting that there is no close genetic and spatial relationship between these porphyries and the mineralization.

### 3.2. Orebodies

The known orebodies (Nos. II, III, IV, VI, IX and M2) in the LAG are vein type (Fig. 4a–c), hosted in the banded siliceous dolomite marble, quartz-bearing dolomite marble and sericite schist of the Meiyaogou and Nannihu formations, as well as within dolomite,

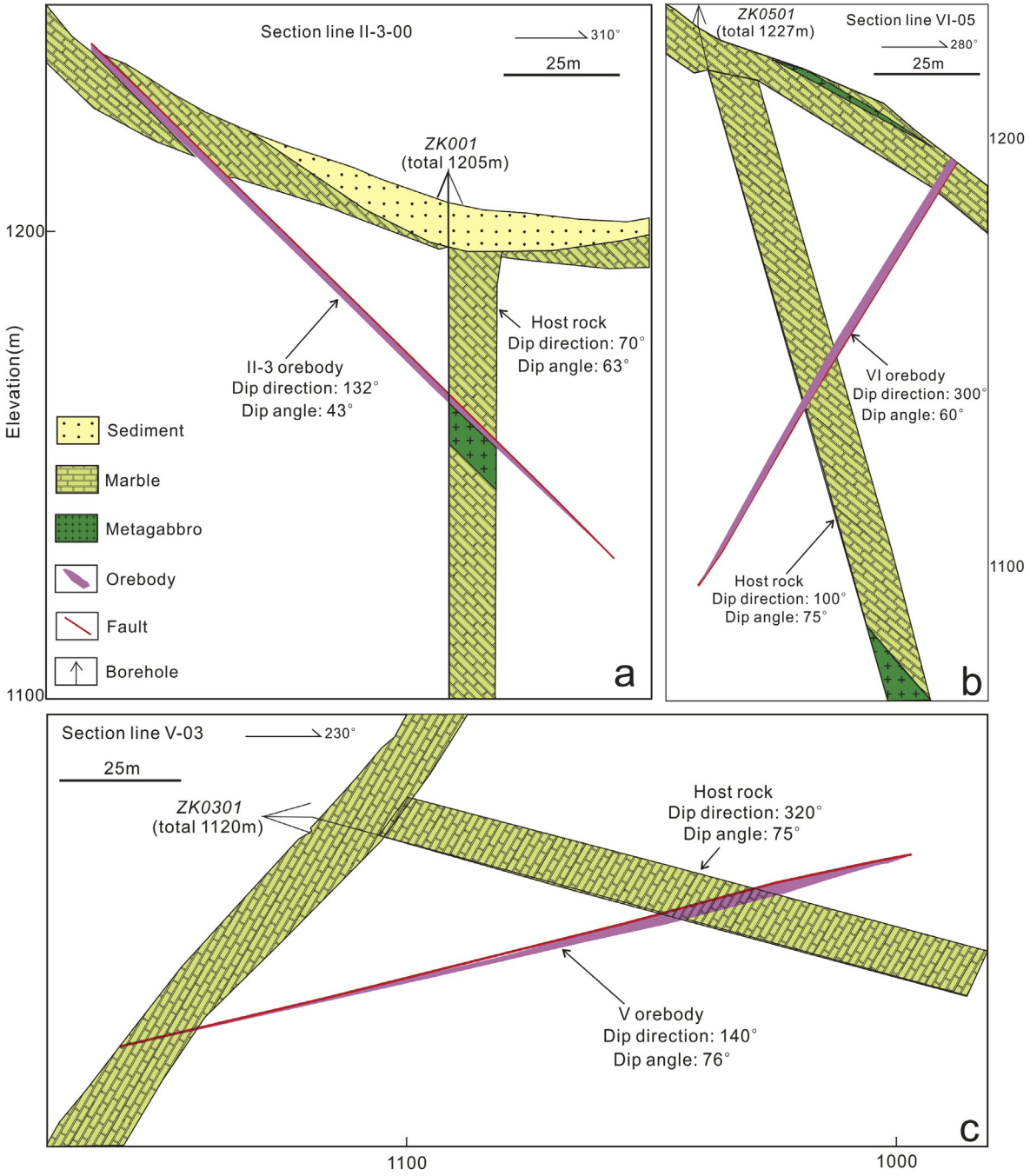


**Fig. 4.** Representative exploration profiles for the No. II orebody (a), No. VI orebody (b) and No. V orebody (c), showing the spatial relationships among metagabbro, orebodies and host rocks (Modified after Guang et al., 2013).

sericite-quartz schist and carbonaceous slate of the Baishugou formation (Fig. 3). The No. III orebody is a concealed orebody and is the main orebody in the LAG (Fig. 3), hosted in the siliceous banded dolomite marble of Baishugou formation, and stretches along a NW-trending fault with dip angles of 50-54°. The M2 orebody is also a concealed orebody and one of the major ones in the LAG (Fig. 3), and hosted in the siliceous banded dolomite marble of Meiyaogou formation, with NE-trend and dipping 42–58°. The No. IX orebody is hosted in dolomite marble and carbonaceous slate of the Baishugou formation, extending NNE and dipping 45–50°, and is located in the same metallogenic belt as No. III orebody, although separated by the NE trending fault (Fig. 3). The No. IV orebody is controlled by secondary structures of the NE-trending fault in the LAG, stretching NE with dip angles of 80°. The Nos. II and VI orebodies are distributed in the Laoangou region, and show NW trend with dip angles of 40–80° (Fig. 4a, b). The No. V orebody is mainly hosted in the marble of Baishugou formation with a dip of 76° (Fig. 4c). Overall, these known orebodies are mainly hosted in banded siliceous dolomite marble and quartz-bearing dolomite marble, which are controlled by NW-, NE- and nearly SN-trending faults in the LAG (Guang et al., 2013; Cao et al., 2015; Yang et al., 2016).

### 3.3. Spatial distribution

The NW-trending faults define the major tectonic feature in the LAG. Most of the orebodies occur along the strata or interlayers within the fracture zone. Particularly, the intersection zone between ore-bearing strata and NE-trending faults host the major orebodies (Guang et al., 2013; Yang et al., 2016). Furthermore, tectonic breccia developed within the fault zones shows a close relationship with Pb-Zn-Ag polymetallic mineralization in the intersection zone, and the dolomite marble is often cemented by sulfides and distributed along NE- or NW-trending faults (Fig. 3).

### 3.4. Paragenetic relationships

The known orebodies in the LAG occur as veins with a thickness of 1–5 m and a length of 0.5–1.0 km, and are mainly hosted in banded siliceous dolomite marble and quartz-bearing dolomite marble (Guang et al., 2013). The boundaries between the orebodies and the wall rocks are sharp (Fig. 5H), and these known orebodies are usually distributed in quartz veins (Fig. 5G, I). The ore minerals are mainly represented by galena, sphalerite, pyrite, and minor amounts of chalcopyrite, tetrahedrite and argentite, whereas the gangue minerals include quartz, dolomite and calcite (Guang et al., 2013; Cao et al., 2015) (Fig. 5A–F). Representative samples (Table 2) collected from fresh surface inside the mine tunnel of the No. III orebody were used for petrologic studies. Sample M01 was taken from wall rock dolomite marble and is characterized by spots of pyrites (Fig. 5A). Sample M03-1 from the No. III orebody contains pyrite, sphalerite and galena as the main ores (Fig. 5B), and sample M03-6 is from a late quartz vein which cuts the wall rock (Fig. 5E, F). The pyrite shows anhedral, euhedral and colloform morphology under the microscope (Fig. 5a–f), and often occur as fillings in quartz veins and is also sporadically distributed in the dolomite marble (Fig. 5a, e, f). Most of the pyrite crystals in the quartz stringers of dolomite marble are euhedral (Fig. 5c, d). However, the sphalerite and galena surrounding the pyrite are anhedral (Fig. 5b, c). The texture suggests that the galena and sphalerite are coeval and formed later than the pyrite. Hence, the Pb-Zn-Ag polymetallic mineralization is inferred to be younger than the early pyrite. In summary, the ores commonly show banding and massive structure, and the minerals in the ores are commonly euhedral-subhedral and medium- or coarse-grained consistent with the results reported by Cao et al. (2015).

Based on the mineral assemblages, textural relationships and data from previous studies (Wang et al., 2013; Guang et al., 2013; Cao et al., 2015; Yang et al., 2016), the hydrothermal-vein (HV) type Pb-Zn-Ag deposits of the LAG can be subdivided into three stages as follows (Fig. 6). The early quartz-pyrite stage (Stage I) typically occurring along both sides of the veins, the quartz–sulfide stage (main stage, stage II) forming sphalerite-galena-quartz assemblage and typically distributed at the center of the veins and the late quartz-carbonate stage (Stage III) mainly including quartz, dolomite and calcite (Fig. 6).

## 4. Methodology

The 3D geological models in this study were constructed from multiple datasets collected from geological data and metallogenic features, including two cross-sections, a 1:10,000 geological map, 39 1:1000 sections of exploration lines, 5 prospects, 66 exploration boreholes, and regional geophysical data (gravity, magnetic and topographic). Subsequently, the 3D modeling and weights of evidence (WofE), Logistic regression, Information entropy and fractal methods were adapted to enable 3D mineral potential targeting by analysis and integration of exploration targeting criteria using various datasets as described in the following sections.

### 4.1. Weights of evidence (WofE) method

The ordinary WofE method is a bivariate statistical approach based on Bayes' theory of conditional probability that quantifies the relationship between mapped distributions of a given dataset and training points, which in this case are areas of known mineralization (Agterberg, 1992, 2011; Bonham-Carter, 1994; Agterberg, 2011; Yuan et al., 2014; Ford et al., 2016), including the ordinary WofE, weighted WofE and boost WofE methods. The data-driven WofE method uses statistics to derive posterior probability values for a given part of the model, which show the probability of a mineral deposit existing (Ford et al., 2016).

In this study, the ordinary WofE method is employed to get posterior probability ($P_{posterior}$) of each block within 3D geological block models of this study and the prior probability ($P_{prior}$) which should be obtained firstly represent the probability of occurrence of a mineral deposit without consideration of any known evidence. For the data of the $i$th binary exploration criterion, $P$ represents the probability, $i$ represents estimated weights of evidence values generated by taking the natural log of the probability ratios, $B_i$ represents the presence of the ith exploration criterion, $\bar{B}_i$ represents the absence of the $i$th exploration criterion, $D$ represents the presence of the mineral deposit, $\bar{D}$ represents the absence of the mineral deposit, $W_i^+$ represents the weight of the presence of exploration criterion, and $W_i^-$ represents the weight of the absence of exploration criterion. $W_i^+$ and $W_i^-$ can be estimated respectively in Eqs. (1) and (2) as follows:

$$W_i^+ = \ln\frac{P(B_i|D)}{P(B_i|\bar{D})} \quad (1)$$

$$W_i^- = \ln\frac{P(\bar{B}_i|D)}{P(\bar{B}_i|\bar{D})} \quad (2)$$

Through computing the contrast $C_i = W_i^+ - W_i^-$, we can obtain the strength of correlation between an exploration criterion and the mineral deposit, which can be tested for statistical significance. Besides, probability can be expressed in terms of odds, and $O_{prior}$ can be estimated as $P_{prior}/(1 - P_{prior})$. The WofE method requires that each exploration criterion in respect to the distribution of the mineral deposit is independent. $\sum_{i=1}^{N} W_i^k$ $(i = 1, 2 \ldots\ldots N)$ represents the weighted accumulation of the $N$ exploration criterion

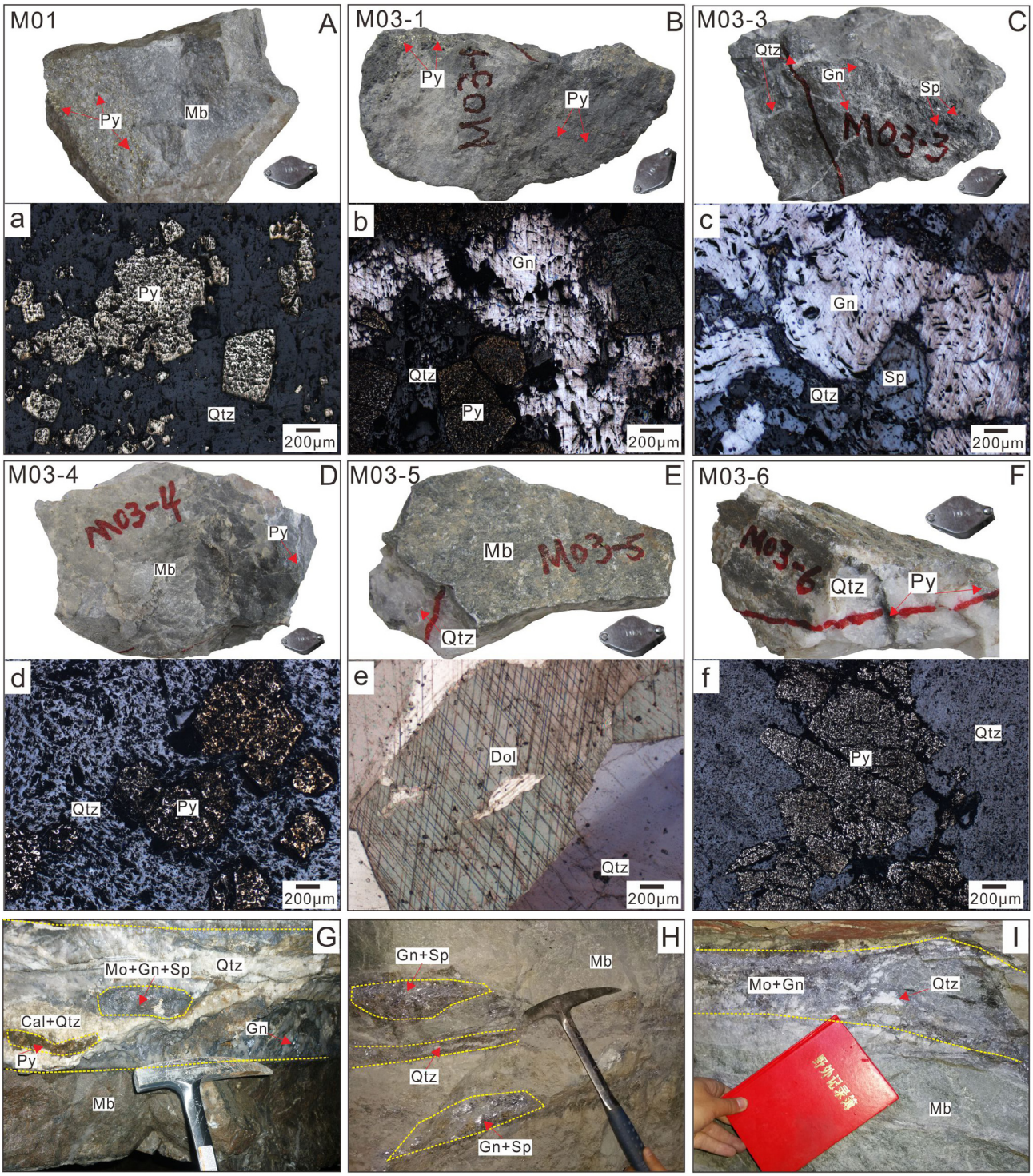


**Fig. 5.** Hand specimen photographs and transmitted light or reflected light photomicrographs of representative mineral assemblages and textural features of the LAG. M01 medium-fine grained pyrites sporadically distributed in marble (A). The pyrites are mainly medium-fine grained (10–600 μm) with subhedral to euhedral structure (a). M03-1 Massive ore, including dark brown medium-fine grained sphalerite, galena and pyrite (B). The pyrites are mainly subhedral to euhedral and medium-fine grained, whereas the medium-fine grained galena shows xenomorphic structure (b). M03-3 Massive quartz veins with sphalerite, galena and pyrite (C). Sphalerite infilling the quartz veins is surrounded by medium to coarse grained galena (c). M03-4 sampled from the walk rock, showing massive structure and carrying quartz veins (D). Medium-fine grained (10–600 μm) subhedral to euhedral pyrite (d). M03-5 quartz veins in the contact zone with marble (E), containing dolomite with two sets of joints and coarse grained quartz (e). M03-6 sampled from quartz veins including pyrites (F). Medium-fine grained pyrite surrounded by xenomorphic quartz (f). Spatial distribution of mineralization within wall rocks in underground exposure of the LAG (G, H and I). Photomicrograph (e) is in reflected light, whereas others (a, b, c, d and f) are in transmitted lights. The longest diameter of mini-magnifier in the photographs is about 2 cm. Abbreviations of minerals: Sp-sphalerite; Mo-molybdenum; Py-pyrite; Gn-galena; Qtz-quartz; Dol-dolomite; Mb-marble; Cal-calcite.

**Table 2**
Locations and characteristics of samples from the LAG.

| Sample No. | Location | Coordinate | Rock type | Sample description |
|---|---|---|---|---|
| M01 | III orebody | N 33°50′30″; E 111°34′18″ | Wall rock | Massive structure, medium-fine grained pyrites sporadically distributed in the dolomitization marble |
| M03-1 | III orebody | N 33°50′30″; E 111°34′18″ | Sphalerite- and galena-bearing ore | Massive ore, dark brown medium-fine grained sphalerite, galena and pyrite |
| M03-3 | III orebody | N 33°50′30″; E 111°34′18″ | Sphalerite- and galena-bearing ore | Massive structure containing many quartz stringers, medium-fine grained anhedral galena and sphalerite |
| M03-4 | III orebody | N 33°50′30″; E 111°34′18″ | Wall rock | Massive structure containing many quartz stringers, medium-fine grained anhedral galena and euhedral pyrite |
| M03-5 | III orebody | N 33°50′30″; E 111°34′18″ | Quartz vein | Quartz vein with brown medium-fine grained calcite and dolomite |
| M03-6 | III orebody | N 33°50′30″; E 111°34′18″ | Quartz vein | Quartz vein, including brown medium-fine grained calcite, with less fine grained pyrite |

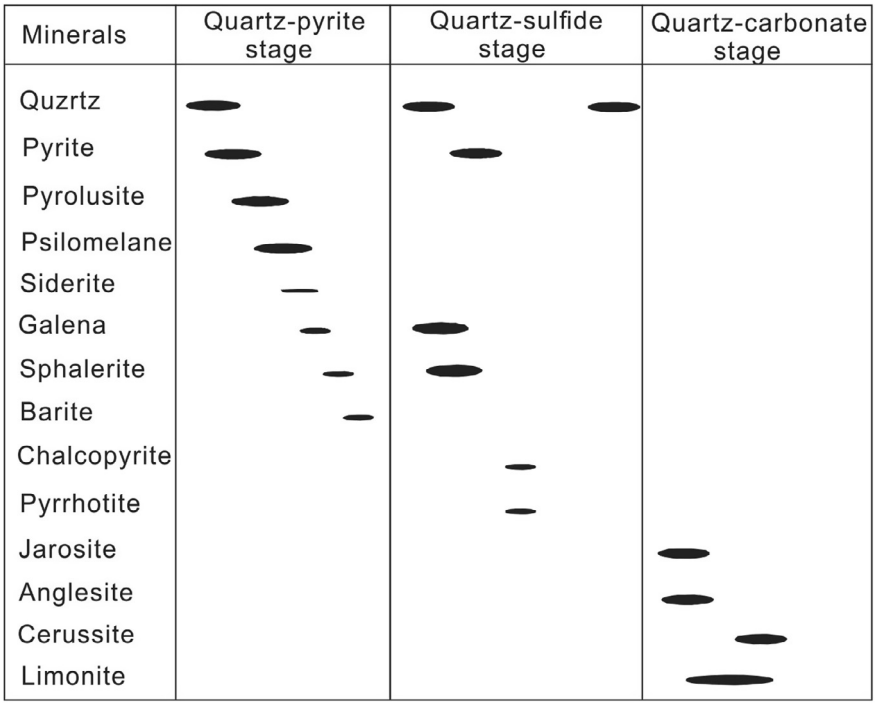


**Fig. 6.** Paragenetic sequences of minerals of the LAG, showing the mineral assemblage and formation sequence during the different metallogenic stages (Modified after Guang et al., 2013; Wang et al., 2013).

within a block in this study, which is linked to the $W_i^+$ when the i-th exploration criterion exists in the block, otherwise it is linked to the $W_i^-$. When the exploration criteria are independent, and then $O_{posterior}$ can be estimated in Eq. (3) as follows:

$$O_{posterior} = O_{prior} * e^{\sum_{i=1}^{N} W_i^k} \quad (i = 1, 2 \ldots\ldots N). \tag{3}$$

Finally, the posterior probability of each block can be obtained by processing data based on Eq. (4) which is the natural logarithm of Eqs. (3) and (5) as follows:

$$lnO_{posterior}(D|B_1^k B_2^k \cdots B_N^k) = lnO_{prior} + \sum_{i=1}^{N} W_i^k \quad (i = 1, 2 \cdots\cdots N) \tag{4}$$

$$P_{posterior} = \frac{O_{prior}}{1 - O_{posterior}}. \tag{5}$$

The weighted WofE method takes into account the modified weights of evidence, which combines the ordinary WofE with weighted logistic regression. It can achieve unbiased estimates of the posterior probabilities while keeping the form of WofE, and cope with missing data on some exploration criteria by setting the weights of unit cells with missing data equal to zero in WofE applications. More detailed description of procedures and method are outlined by Agterberg (2011).

The boosted WofE method is a new form of weights of evidence model, and can integrate binary exploration criteria in sequence with updates, within dependent weights for the first exploration criterion and the conditional weights for the subsequent exploration criteria (Li et al., 2016). The boosted WofE is more generic and does not rely on other models and later corrections compared with other techniques of handling conditional dependency (Cheng, 2015). The detailed description of boosted WofE method has been outlined by Cheng (2012).

### 4.2. Logistic regression method

The logistic regression method was formulated and applied to different case studies by Chung and Agterberg (1980). This method is mainly applied to describe the relationship between a response variable which must be binary or dichotomous and one or more

predictor variables (Chung and Agterberg, 1980; Harris and Pan, 1999; Carranza and Hale, 2001; Menard, 2001; Hosmer and Lemeshow, 2004). The response variable in logistic regression must be binary or dichotomous unlike in linear regression models (Chung and Agterberg, 1980; Carranza and Hale, 2001; Dai and Lee, 2002; Hosmer and Lemeshow, 2004; Ayalew and Yamagishi, 2005). The purpose of the Logistic regression is to determine the best fitting model to describe the relationship between the dependent variable and set of independent parameters (Kavzoglu et al., 2014). An additional advantage of Logistic regression is that it need not satisfy the assumption of conditional independence, and can provide true conditional probabilities even if the joint distribution of predictors and the response variable is of log-linear form (Carranza and Hale, 2001; Akgun, 2012; Schaeben, 2014; Zhang et al., 2014). The approach is based on the following equations:

$$P = 1/(1 + e^{z}) \tag{6}$$

In the Eq. (6), P represents the probability of an event, and Z is a value from $-\infty$ to $+\infty$ which is defined by the Eq. (7) as follow:

$$Z = B_0 + B_1X_1 + B_2X_2 + \cdots + B_nX_n \tag{7}$$

In the Eq. (7), $B_0$ represents the intercept of model, n represents the number of independent variables, and $B_1$, $B_2$,..., $B_n$ represent coefficients which measure the contribution of independent variables ($X_1$, $X_2$, ..., $X_n$) (Ayalew and Yamagishi, 2005; Akgun, 2012). Moreover, the dependent variable in the Logistic regression method can be expressed into the equation as follow:

$$\begin{aligned}\text{Logit}(p) &= \ln(p/(1-p)) \\ &= 1/1 + e^{-}B0 + B1X1 + B2X2 + \cdots + BnXn\end{aligned} \tag{8}$$

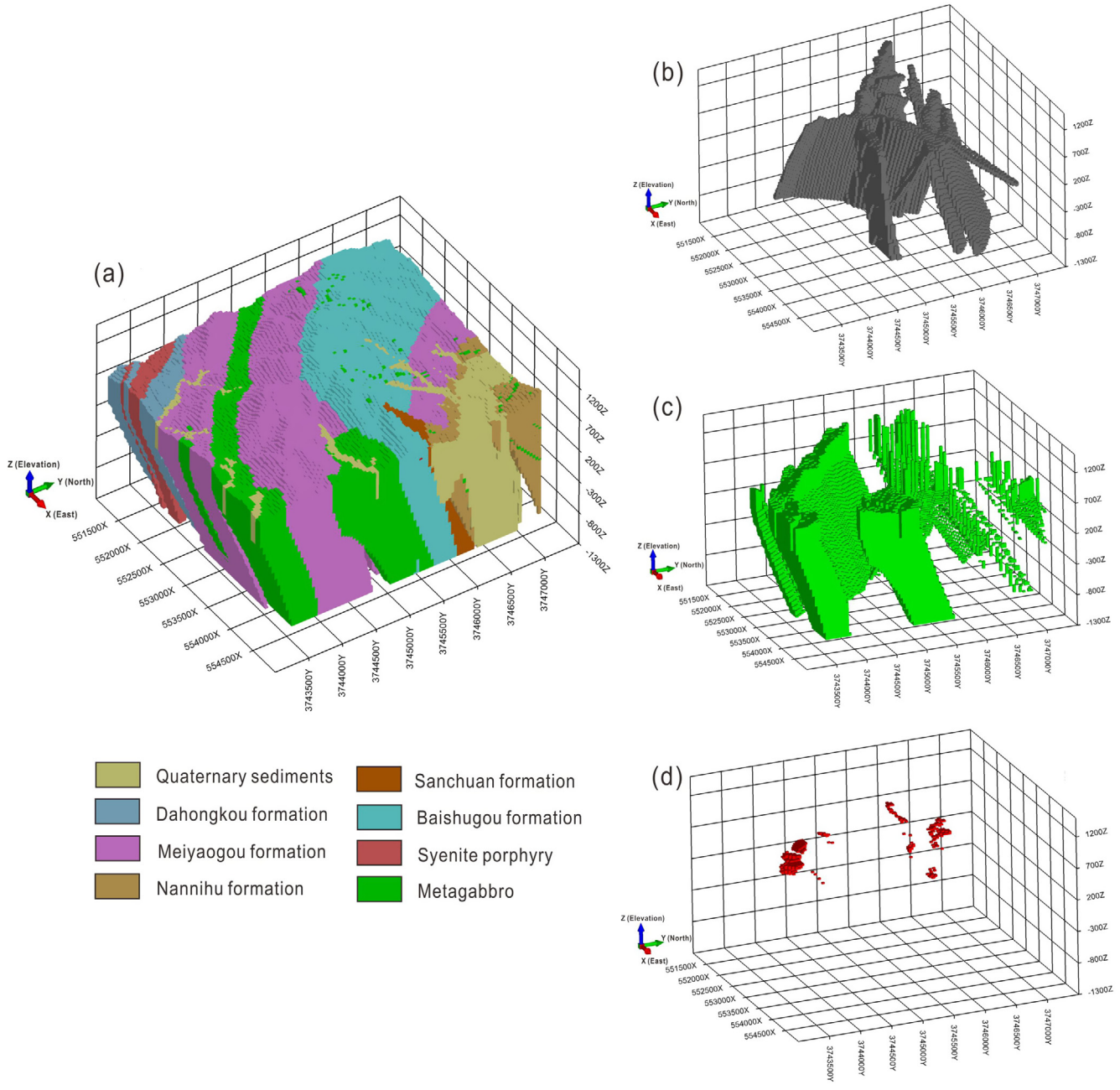


**Fig. 7.** 3D block model of exploration criteria using the Micromine software: (a) strata model, (b) fault model, (c) metagabbro body model, (d) orebody model.

In the Eq. (8), p represents the probability that the dependent variable has values of only 0 and 1 and p/(1 − p) represents odds or likelihood ratio, and the probabilities vary between 0 and 1. If a probability gets closer to 1, the numerator of the odds becomes larger relative to the denominator, and the odds become an increasingly large number. In contrast, when a probability gets closer to 0, the numerator of the odds becomes smaller relative to the denominator (Ayalew and Yamagishi, 2005).

### 4.3. Information entropy method

Information entropy method was firstly defined by Shannon (1948) for identifying the amount of information required to transmit English text. The underlying concept is that, given the probabilities of letters in the English alphabet, it is possible to derive a measure describing the missing information to determine the full text of a partially transmitted message where information is understood as the information required to identify the message, not the information of the message itself (Wellmann and Regenauer-Lieb, 2012). Accordingly, a new equation based on several theoretical considerations was proposed to classify a measure of the missing information which is generally referred to as the Information entropy method (Shannon, 1948):

$$H = -\sum_{i=1}^{N} P_i \log P_i. \quad (9)$$

In the Eq. (9), the information entropy H represents the sum of all products of probabilities p for each possible outcome i of N total possible outcomes with its logarithm. The minimum value is 0, since $\log 1 = 0$ and $\lim x \to 0 (x \log x) = 0$ (Ben-Naim, 2008; Wellmann and Regenauer-Lieb, 2012).

Recently, the Information entropy method involving statistical analysis, has been applied to regional mineral prediction field, is also a statistical analysis method (Vysokoostrovskaya and Zelenetsky, 1968; Wellmann and Regenauer-Lieb, 2012; Li et al., 2016). This technique can determine the favorable location for mineralization by calculating the geological factors and prospecting indicators, and evaluate quantitatively each exploration criterion to further guide prospecting work (Li et al., 2016).

### 4.4. Fractal method

The concentration-area (C-A) fractal method is mainly used for defining backgrounds and anomalies (Cheng et al., 1994). Based on the analyses of C-A fractal method, the background obeys normal distribution and lognormal distribution, and the anomalies may relate to a fractal distribution. The fractal model can be defined as follows:

$$N(r) = Cr^{-D}.. \quad (10)$$

$$LnN(r) = lnc - Dlnr \quad (11)$$

In Eqs. (10) and (11), r is the characteristic exponent that involves the posterior probability in one case. N(r) is the number of unit cells for which posterior probability is equal to or less than r. *C* is the proportionality coefficient, and *D* is the fractal dimension, $\ln r$ is linearly associated with $\ln N(r)$. The piecewise fitting of straight lines can be obtained by applying least squares. The points

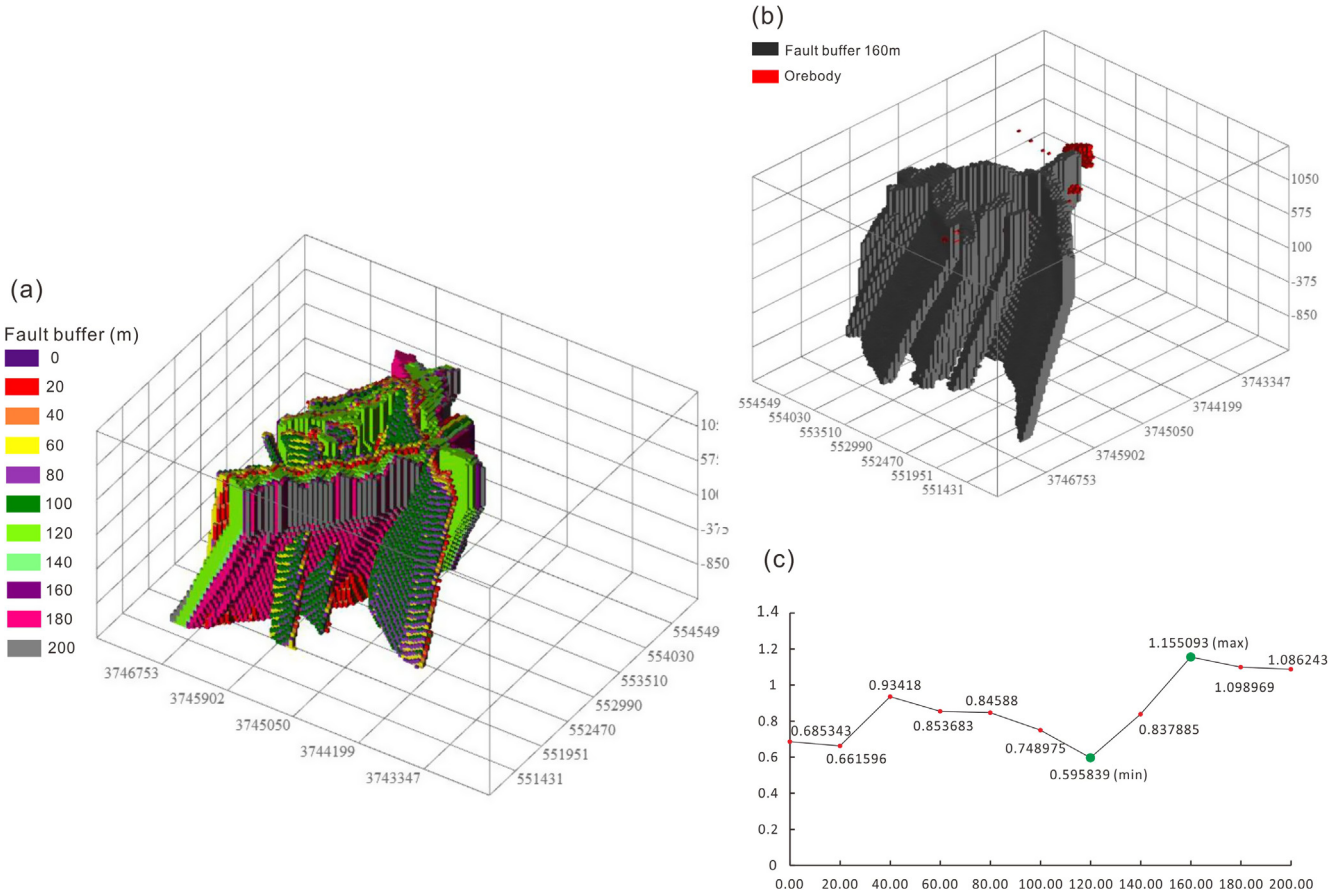


**Fig. 8.** 3D block model of fault exploration criteria computed using the Geocube software. (a) Fault buffering model from 20 m to 200 m, (b) 3D orebody model and 160 m buffer fault model, (c) curve plot of buffering fault using the method of WofE.

**Table 3**
List of parameters for various exploration criteria based on the weights of evidence model. Implication: N(E) – unit cells number of evidence factor; N(D) – unit cells number of mineral deposits; $W^+$ – positive weights of evidence; $W^-$ – negative weights of evidence; $s(W^+)$ – standard deviations of $W^+$; $s(W^-)$ – standard deviations of $W^-$; C – spatial contrast; s(C) – standard deviation of C; Studentized(C) – studentized contrast. Strata abbreviations: PT3M, Meiyaogou formation; PT3B, Baishugou formation; PT3S, Sanchuan formation.

| Exploration criteria | N (E) | N (D) | $W^+$ | s ($W^+$) | $W^-$ | s ($W^-$) | C | s (C) | Studentized (C) |
|---|---|---|---|---|---|---|---|---|---|
| Magnetic anomaly | 42541 | 171 | 1.920187 | 0.076626 | −0.44276 | 0.061792 | 2.36295 | 0.098437 | 24.00474 |
| Electrostatic anomaly | 8499 | 39 | 2.053176 | 0.160497 | −0.08276 | 0.050393 | 2.135937 | 0.168222 | 12.69713 |
| Pb anomaly | 9855 | 34 | 1.766801 | 0.171795 | −0.06827 | 0.050076 | 1.835069 | 0.178945 | 10.25494 |
| Zn anomaly | 16741 | 30 | 1.110094 | 0.182738 | −0.04871 | 0.049828 | 1.158799 | 0.18941 | 6.117957 |
| Fault-buffer-160m | 84365 | 126 | 0.927587 | 0.089154 | −0.22162 | 0.057087 | 1.149208 | 0.105864 | 10.85549 |
| PT3M2 | 129194 | 163 | 0.758661 | 0.078376 | −0.27838 | 0.060872 | 1.037045 | 0.099238 | 10.45013 |
| PT3M3 | 92317 | 77 | 0.344375 | 0.114008 | −0.06111 | 0.053015 | 0.405483 | 0.125731 | 3.224994 |
| PT3B3 | 239186 | 152 | 0.072238 | 0.081136 | −0.037 | 0.059672 | 0.109243 | 0.100717 | 1.084651 |
| PT3S | 6276 | 3 | −0.21268 | 0.577488 | 0.001655 | 0.048239 | −0.21433 | 0.5795 | −0.36986 |
| Metagabbro | 95975 | 33 | −0.54227 | 0.174108 | 0.06123 | 0.050016 | −0.6035 | 0.181149 | −3.33152 |
| Rock | 169390 | 24 | −1.42905 | 0.204139 | 0.206152 | 0.049465 | −1.6352 | 0.210046 | −7.78495 |
| PT3M1 | 80131 | 4 | −2.47236 | 0.500012 | 0.10666 | 0.048296 | −2.57902 | 0.50234 | −5.13401 |

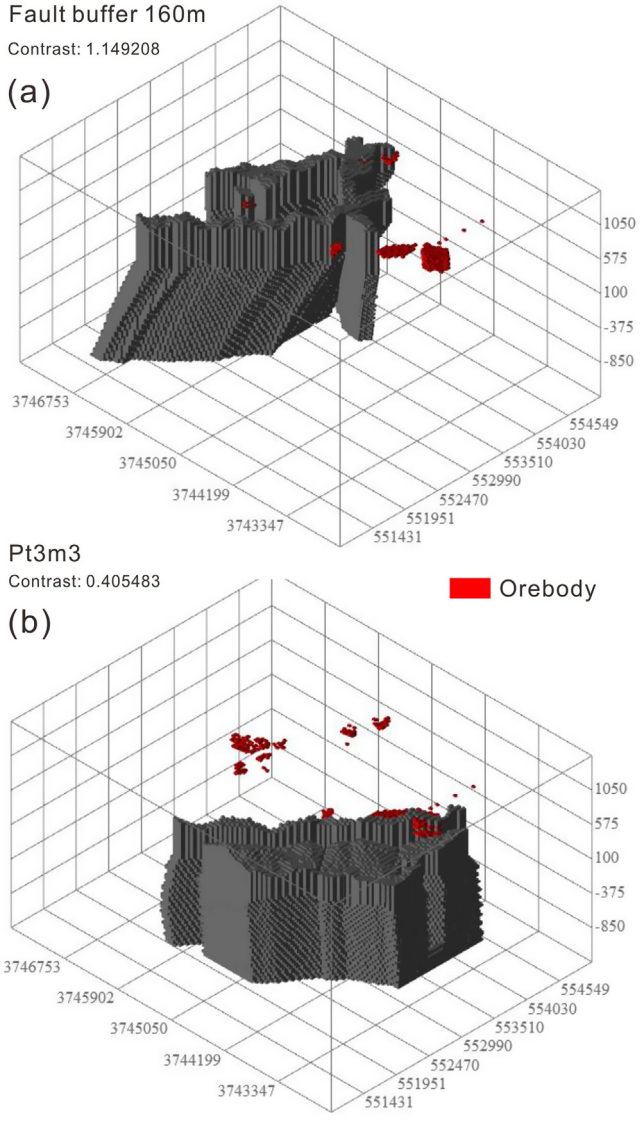


**Fig. 9.** Intersection of exploration criteria and the 3D orebody model of the LAG. Strata abbreviations: PT3M, Meiyaogou formation; PT3B, Baishugou formation; PT3S, Sanchuan formation.

demarcating adjacent straight lines are considered cutoff values separating background and prospect areas of different levels of potentiality (Cheng et al., 1994; Li et al., 2015a).

## 5. 3D exploration criteria modeling

Exploration criteria selected in this study are based on metallogenic theory and deposit-scale model of the hydrothermal-vein type Pb-Zn-Ag polymetallic ore deposits (Wang et al., 2013; Cao et al., 2015). The strata, ore-controlling fault and known orebodies are the most important exploration criteria in the LAG (Fig. 7). Through combining the results from this study with those from previous work (Guang et al., 2013; Wang et al., 2013, 2017; Cao et al., 2015; Yang et al., 2016), the metagabbro bodies exposed in the deposit and the geophysical anomalies can be regard as exploration criteria for indirectly guiding deep prospecting work.

### 5.1. Strata modeling for exploration criteria

The procedure of 3D strata model (Fig. 7a) of the LAG was constructed as follows (Wang et al., 2015). (1) Application of 1:10,000 scale geological map, two cross-sections and 39 sections of prospecting line; (2) Combining the 3D fault model using Wireframe connection and Boolean operation function using Micromine software; and (3) optimization of the model by data from boreholes. According to the analyses of the known orebodies, 3D spatial analysis can successfully extract information on ore-controlling strata to build the block model (Wang et al., 2015). The strata exposed in the LAG mainly include the Baishugou formation of Guandaokou group and Dahongkou, Meiyaogou, Nannihu and Sanchuan formations of Luanchuan group (Fig. 3). Among these, the Meiyaogou and Baishugou formations are associated with Pb-Zn-Ag polymetallic mineralization, and therefore they can be regarded as the main ore-controlling exploration criteria for modeling of potential exploration targets.

### 5.2. Fault modeling for exploration criteria

The fault model (Fig. 7b) constructed in the LAG mainly incorporates the fault lines from 1:10,000 scale geological map. They are controlled by the cross-sections, and used for 3D buffer analysis using the Geocube software (Li et al., 2016). The method of weights of evidence (WofE) is used for constructing a curve for determining an optimum buffer distance (Fig. 8c). Fig. 8a shows the buffer fault model from 20 m to 200 m, and Fig. 8b shows that at 160 m and 3D orebody model. Fig. 8c shows the results of the calculation. The C parameter of the calculation result (Fig. 8c) has a minimum value for the 120 m buffer and maximum value for the 160 m buffer for all the faults. Previous studies on the hydrothermal-vein type Pb-Zn-Ag polymetallic ore deposits in the LOD shows that the ore-controlling fault has influenced the formation of the orebody to 200 m (Guang et al., 2013; Wang et al., 2015), which is a key exploration criterion for Pb-Zn-Ag. Thus, we choose the value of the 160 m buffer around faults which is1.155 (max) as the exploration criteria (Fig. 8c).

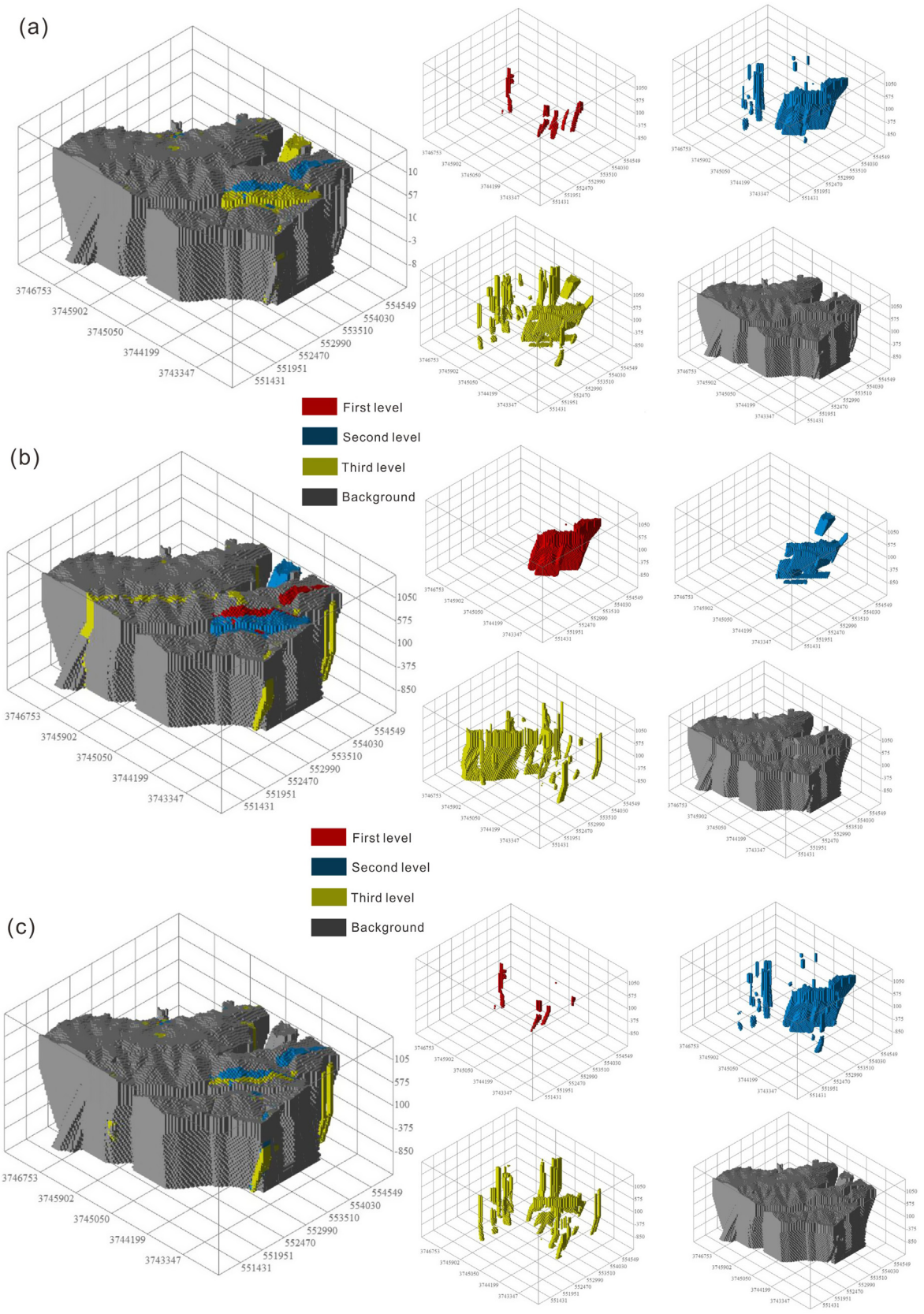


**Fig. 10.** 3D exploration targets model. a: ordinary WofE model; b: boost WofE model; c: weighted WofE model.

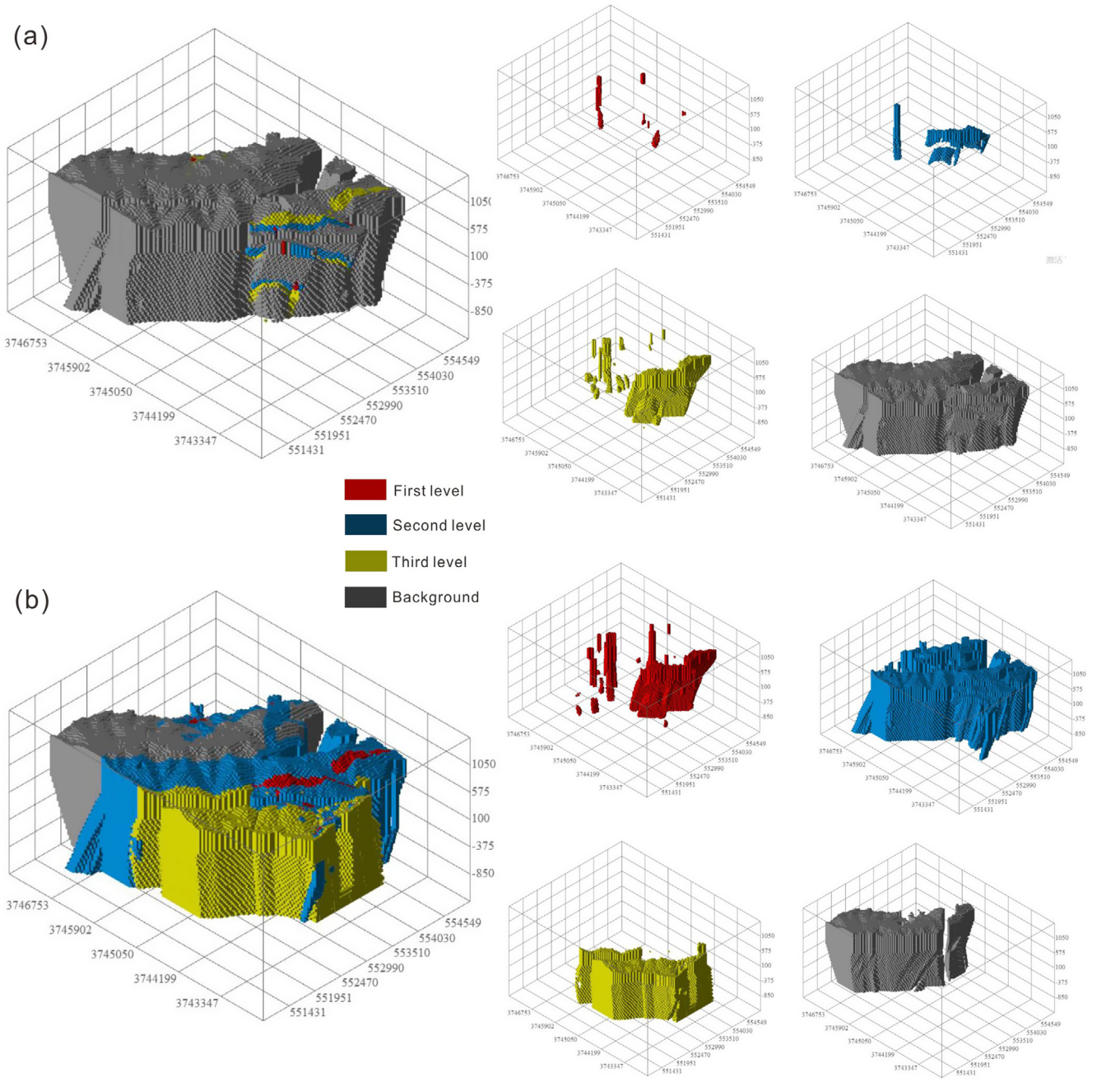


**Fig. 11.** 3D exploration targets model. a: logistic regression model; b: information entropy model.

### 5.3. Modeling the metagabbro bodies for exploration criteria

The model for metagabbro in the ore deposit (Fig. 7c) was constructed in two steps: at first the 3D model for metagabbro body was constructed based on the distribution of the outcrop, followed by modeling using Micromine software through application of Wireframe connection and Boolean operation function. The 3D spatial analysis was also applied to extract the 3D model of metagabbro body and to create the block model. Many metagabbro dykes are exposed on the surface around the LAG (Fig. 3), and almost all the exploration profiles in the LAG also show the occurrence of metagabbro dykes at depth (Fig. 4). The known orebodies show clear spatial relationship with the metagabbro dykes (Figs. 3 and 4), suggesting a spatial relationship with the orebodies (Fig. 4). Moreover, previous studies in the LAG have also confirmed a close relationship with the Pb-Zn-Ag mineralization (Guang et al., 2013; Yang et al., 2016). Hence, the metagabbro bodies can be regarded as the indirect indicators of the distribution of orebodies.

### 5.4. Known orebody modeling for exploration criteria

The known orebody model in the LAG (Fig. 7d) was constructed through the following steps. (1) Application of 1:1000 scale geological map for extracting the outcrop profile of orebodies; (2) using 39 sections of exploration lines for outlining the orebodies; and (3) delineation the outline of orebodies based on 66 boreholes. The 3D spatial analysis was also applied to extract the 3D model of known orebodies and to create the block model. Furthermore, Wang et al. (2017) proposed that the orebody-scale models of large

deposit can be employed to validate and assess the uncertainty in both the deposit- and district-scale models in the LOD.

## 6. Exploration criteria extraction and integration, and potential target delineation

### 6.1. Exploration criteria extraction and integration

Based on the models constructed for the LAG, the binary exploration criteria is developed for the LAG taking into consideration the strata, rock, buffer of fault, Zn anomaly, Pb anomaly, magnetic anomaly and induced polarization anomaly. The results of calculation using Geocube software (Li et al., 2016) are listed in Table 2. The contrast C in Table 3 is a statistical parameter which can be used for measuring the correlation between exploration criteria and mineral deposits. If the value of C is above zero, positive correlation between an exploration criterion and the LAG is indicated. Conversely, if the value of C is below zero, a negative correlation is suggested. Besides, the studentized C, which is the ratio of C to its standard deviation, is a useful measure of statistical significance of the contrast, can determine the cutoff levels to convert multi-class or continuous data into binary exploration criterion (Bonham-Carter et al., 1988; Li et al., 2016).

Accordingly, eight exploration criteria listed in Table 3 show statistically significant positive correlations with the LAG. Through the contrast and analyses of each exploration criteria, Fig. 9 shows the intersections of the representative exploration criteria (fault buffer 160 m, Fig. 9a; strata of Pt3m3, Fig. 9b) with the LAG. As shown in Table 3 and Fig. 9, the studentized contrast shows positive correlation with the number of spatial units of intersections between exploration criteria and mineral deposits (N(D)), and negative correction with the number of spatial units of exploration criteria (N(E)). Although the results of integration of exploration criteria do not represent the whole ore district, the intersections of all these are valid exploration criteria.

### 6.2. Potential target delineation

Based on the methods of ordinary WofE, boost WofE, weighted WofE, logistic regression and information entropy, five prediction results were obtained in this study (Figs. 10 and 11). Through comparison and analysis of these results, we conclude that all the three level targets occur in the Meiyaogou and Baishugou formations and the fault zones. However, the five prediction results obtained in this study have significant difference, so that we are not able to confirm which prediction result is more reliable. Accordingly, through calculating the average value of the posterior probability and integrating these results, a new comprehensive prediction model was obtained, where the posterior probability varies from 0.028 to 0.815 (Table 4). Generally, the C–V fractal method is used for separating the prospect areas from background and further classifying the results of WofE (Li et al., 2016; Wang et al., 2015, 2017). In this study, three levels of prospecting targets can be identified based on this method of the C–V fractal (Fig. 14). Fig. 12 shows the fitted line segments of prospect areas, which is further

**Table 4**
The classification of posterior probabilities based on integrating different methods.

| Class | Interval | Fractal dimension | Goodness-of-Fit |
|---|---|---|---|
| Classification I | [0.162014, 0.815174] | 0.004025 | 0.663865 |
| Classification II | [0.099033, 0.162014] | 0.076691 | 0.898721 |
| Classification III | [0.083863, 0.099033] | 0.827512 | 1.000000 |
| Background | [0.028292, 0.083863] | 0.001611 | 0.291784 |

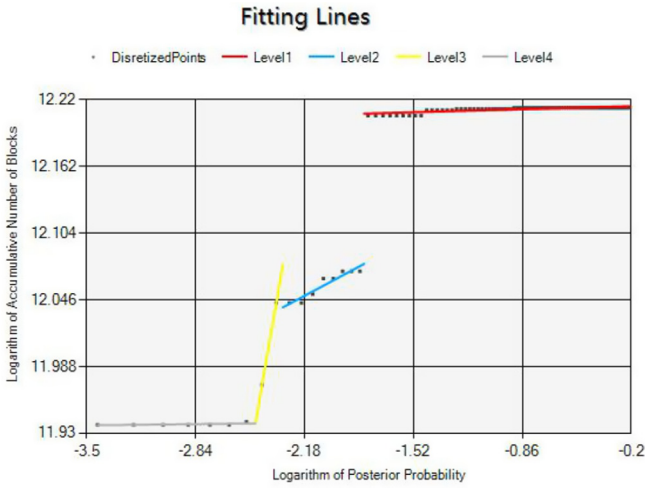


**Fig. 12.** Log–log C–V plots and line segments fitted using least-squares fitting method.

subdivided into three parts. Fig. 13b, c and d are three classes of targets in the LAG, Fig. 13e is the background zone depicting non-potential target, and Fig. 13a is the comprehensive model for prediction within the three delineated targets and background zone.

As shown in Fig. 13, three levels of prospecting targets are clearly delineated. Among these, the first level targets are mainly distributed in the periphery of known orebody (M2, M3, II-3 and VI) (Fig. 13b), which are also located in the ore-controlling strata and fault zones; the second level targets are located in the known ore district (Fig. 13c), which do not provide further guidelines for prospecting, although they confirm that the prediction result is reliable; the third level targets, which are mainly located at the contact between ore-controlling strata and metagabbro (Fig. 13d), represent a new target exploration zone in the LAG.

## 7. Discussion

### 7.1. Analysis of different methods

The WofE method based on Bayesian conditional probability, which is widely used for linear model in mineral prospectivity mapping, determines the optimum binary exploration criteria of a geological feature showing spatial association with a set of mineral deposits (Agterberg, 1989; Bonham-Carter et al., 1989). The spatial association based on the WofE method is correlated with the prior probability of occurrence of the targeted mineral deposits using Bayes' rule in a (log)-linear form under the assumption of conditional independence of the input maps to derive posterior probability of occurrence of the targeted mineral deposits (Porwal et al., 2010). Although most of the WofE methods are mainly used for mineral prospectivity mapping in 2D space, a few recent studies have attempted to use the WofE method in the 3D space (Li et al., 2016; Wang et al., 2015, 2017). Simultaneously, a new approach that combines legacy geological data with 3D spatial analysis and weights of evidence modeling which can identify the controls on mineralization within known orebodies and can be employed to more effectively target areas for future mineral exploration as proposed by Yuan et al. (2014). The C-A fractal method is mainly used for defining backgrounds and anomalies in 2D space (Cheng et al., 1994). Afzal et al. (2011) applied the C–V fractal model in 3D space, and demonstrated the C–V fractal model in 3D space for distinguishing between supergene and hypogene mineralized zones as well as barren host rocks

in the Chah-Firouzeh and Sungun porphyry Cu deposits. Wang et al. (2015) also used the C–V fractal model to identify in 3D space Mo mineralization, orebodies in the LOD. The deposit-scale metallogenic model obtained in this study is primarily based on geological mapping, cross-section construction and borehole intercepts which were used for extracting spatial features and to formulate exploration criteria from geological information in the LAG. The new method based on integrating ordinary WofE, weighted WofE, boost WofE, logistic regression and information entropy was applied to predict the target, whereas the C–V fractal method was used to integrate these spatial features for exploration targeting and classification of probabilities. The C–V log–log plot (Fig. 12) of the LAG reveals a multifractal model which fits with the real situation and three level targets can be obtained from the deposit-scale metallogenic model. Combination of the analysis with application of different methods above provides a feasible approach for

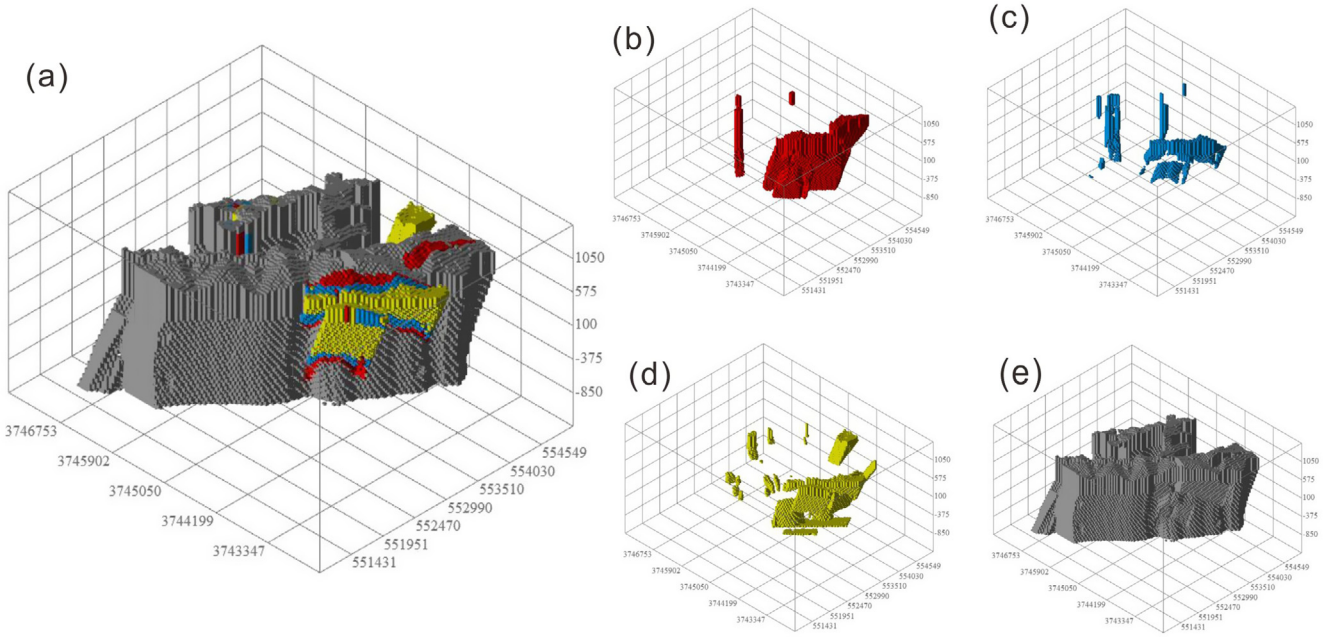


**Fig. 13.** 3D comprehensive exploration targets model based on the methods of ordinary WofE, weighted WofE model, boost WofE, logistic regression and information entropy (a); first level exploration targets (b); second level exploration targets (c); third level exploration targets (d); background zones (e).

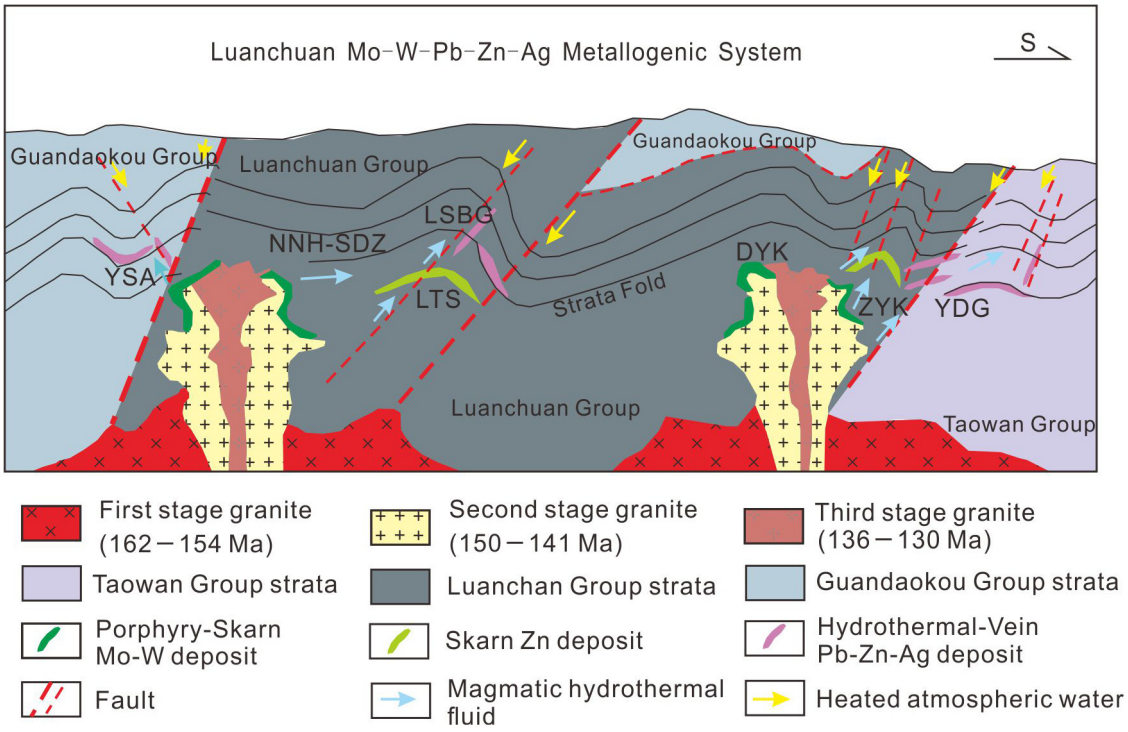


**Fig. 14.** Schematic model of the Luanchuan Mo-W-Pb-Zn-Ag metallogenic system (Modified after Cao et al., 2015; Yang et al., 2016). Abbreviations: DYK, Dongyuku; HDG, Hongdonggou; LSBG, Lengshuibeigou; LTS, Luotuoshan; NNH, Nannihu; SDZ, Sandaozhuang; YDG, Yindonggou; YSA, Yangshuao; ZYK, Zhongyuku.

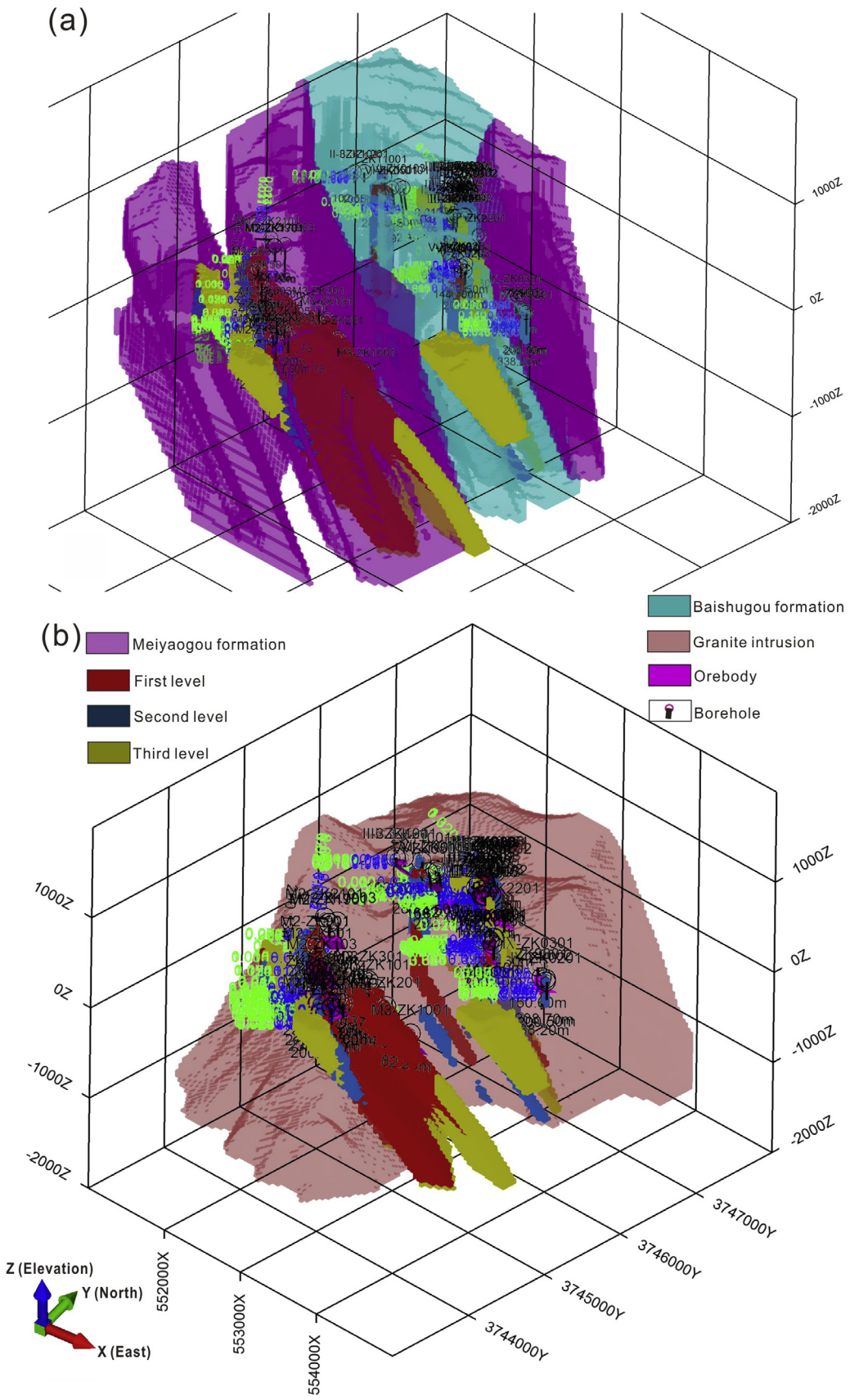


**Fig. 15.** Validation of 3D exploration targets model based on boreholes and strata (a); and validation based on granite rock (b).

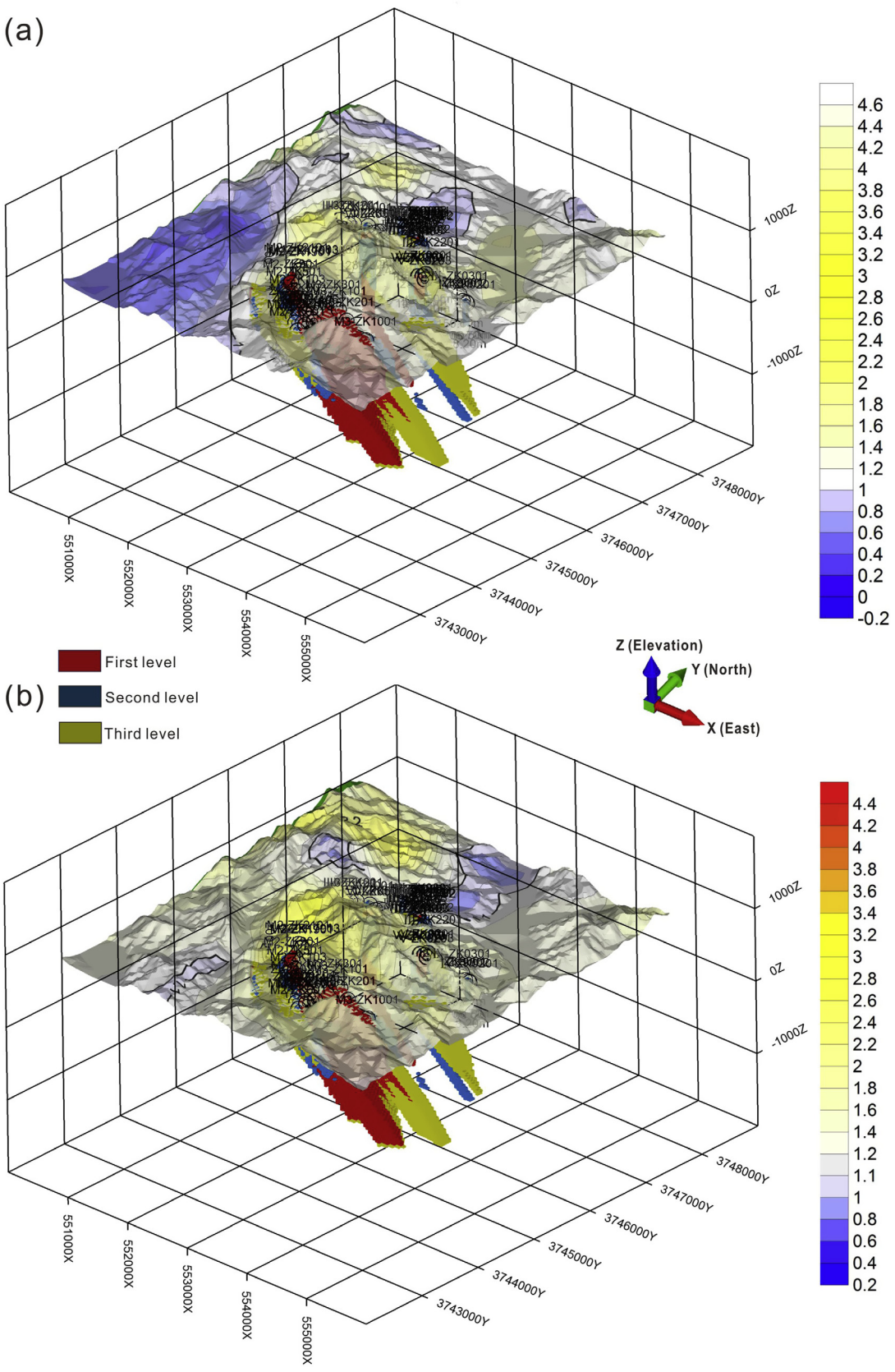


**Fig. 16.** 3D exploration targets model validation. Validation based on Pb element anomaly geochemical map (a); validation based on Zn element anomaly geochemical map (b).

logical 3D metallogenic prediction for guiding future deep exploration.

Moreover, several previous studies have successfully applied these methods for conducting metallogenic prediction, leading to favorable metallogenic zones for further guiding the prospecting work (Yuan et al., 2014; Li et al., 2015a, 2016; Wang et al., 2015, 2017). Above all, the deposit-scale metallogenic model obtained in this study not only depends on integrating the prediction results from five different methods, but also through calculating an average value of the posterior probability from the five different methods. Hence, the comprehensive prediction result is obtained in this study, which is more reliable than those from the individual methods.

### 7.2. Validation of mineral potential target

The Pb-Zn ore deposits in the LOD can be classified into two types: (1) distal hydrothermal-vein (HV) Pb-Zn-Ag deposits which is controlled by regional NW and NS trending faults; (2) intermediate skarn (SK) type Zn deposits distributed at the contact of the Jurassic granite porphyry intrusion (Duan et al., 2010; Wang et al., 2013; Li et al., 2015b; Cao et al., 2015; Yang et al., 2016). Based on the distance from the Jurassic intrusive granite porphyry in region, three types of deposits are identified in the LOD, including the proximal porphyry-skarn (PS) type Mo-W deposits distributed in the inner and outer contract zones, followed by the intermediate skarn (SK) type Zn deposits located in the wall rock of skarn away from the contact zone of the intrusion and the distal hydrothermal-vein (HV) type Pb-Zn-Ag deposits formed in the fault zone of peripheral porphyry (Fig. 14). 3D comprehensive metallogenic model of mineral potential targets are validated based on geological features (strata, rock, geochemical anomaly map and regional fault pattern) associated with the mineralization in this study (Figs. 15–17). As is shown in Fig. 15, the three levels of potential targets are located in the Meiyaogou and Baishugou formations which are the important ore-controlling strata (Fig. 15a). Furthermore, the three level targets are also distributed in the outer zone of the granitic intrusion (Fig. 15b), and the fault zones which away from the granite rock. In summary, the mineral potential targets obtained in this study conform to the regularity of distribution of the hydrothermal-vein Pb-Zn-Ag deposit, suggesting that the prediction results are reliable (Wang et al., 2013; Li et al., 2015b; Cao et al., 2015; Yang et al., 2016). Moreover, combining the geochemical exploration anomaly data on Pb and Zn (Li et al., 2015b), models of validation (Fig. 16a and b) are constructed. The Pb anomaly where the potential targets are distributed is between 1.4 and 3.0 (Fig. 16a), and that of Zn are between 1.8 and 3.4 (Fig. 16b). From Fig. 17a and b, these delineated exploration targets are mainly located in the fault zone, especially at the intersections between NW- and NE-trending faults. Thus, the mineral potential targets obtained are more robust and can further guide the deep prospecting work.

### 7.3. Correlation with previous studies within the LOD

Recently, Wang et al. (2015) carried out the district-scale 3D metallogenic prediction for subsurface Mo targets in the LOD, and obtained four classes of exploration targets based on the integration of 3D exploration criteria as: ore-forming anomalous gravity and magnetic zones, Jurassic granite porphyry bodies, and faults and strata through boosted WofE and C–V fractal methods. In another study, district-scale 3D metallogenic prediction for subsurface Pb-Zn-Ag targets in the LOD was performed by Yang (2016), and identified three classes of exploration targets (A, B and C). Fig. 18a and b respectively show the three classes of exploration targets and their sub-divisions (A, 3; B, 4; and C, 3) based on the three classes of exploration targets in the 3D space (Yang, 2016). From the presented 3D exploration targets related to the Pb-Zn deposits in the LOD (Yang, 2016) (Fig. 18), we identify the LAG is as an A class of exploration target (Fig. 18), further attesting to the possibility of Pb-Zn ores. Furthermore, the district-scale 3D metallogenic prediction also suggests the feasibility of these studies, and their usefulness in conducting the 3D prediction work in the LAG.

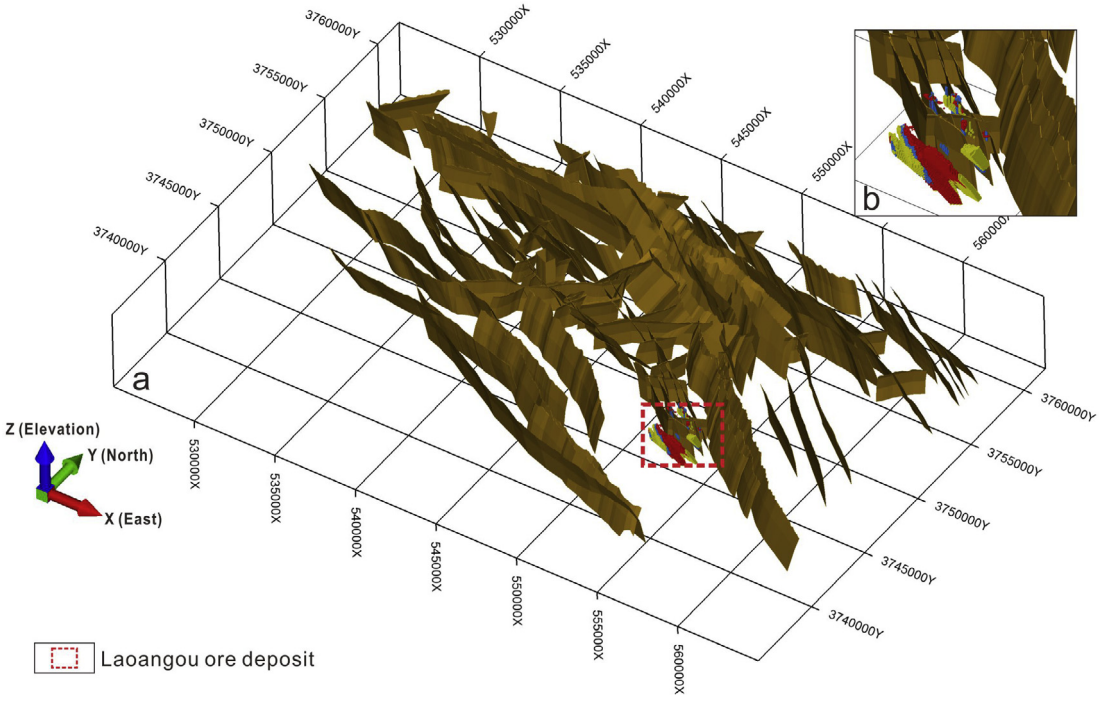


**Fig. 17.** 3D exploration targets model validation. Validation based on regional faults (a and b) (Modified after Wang et al., 2015).

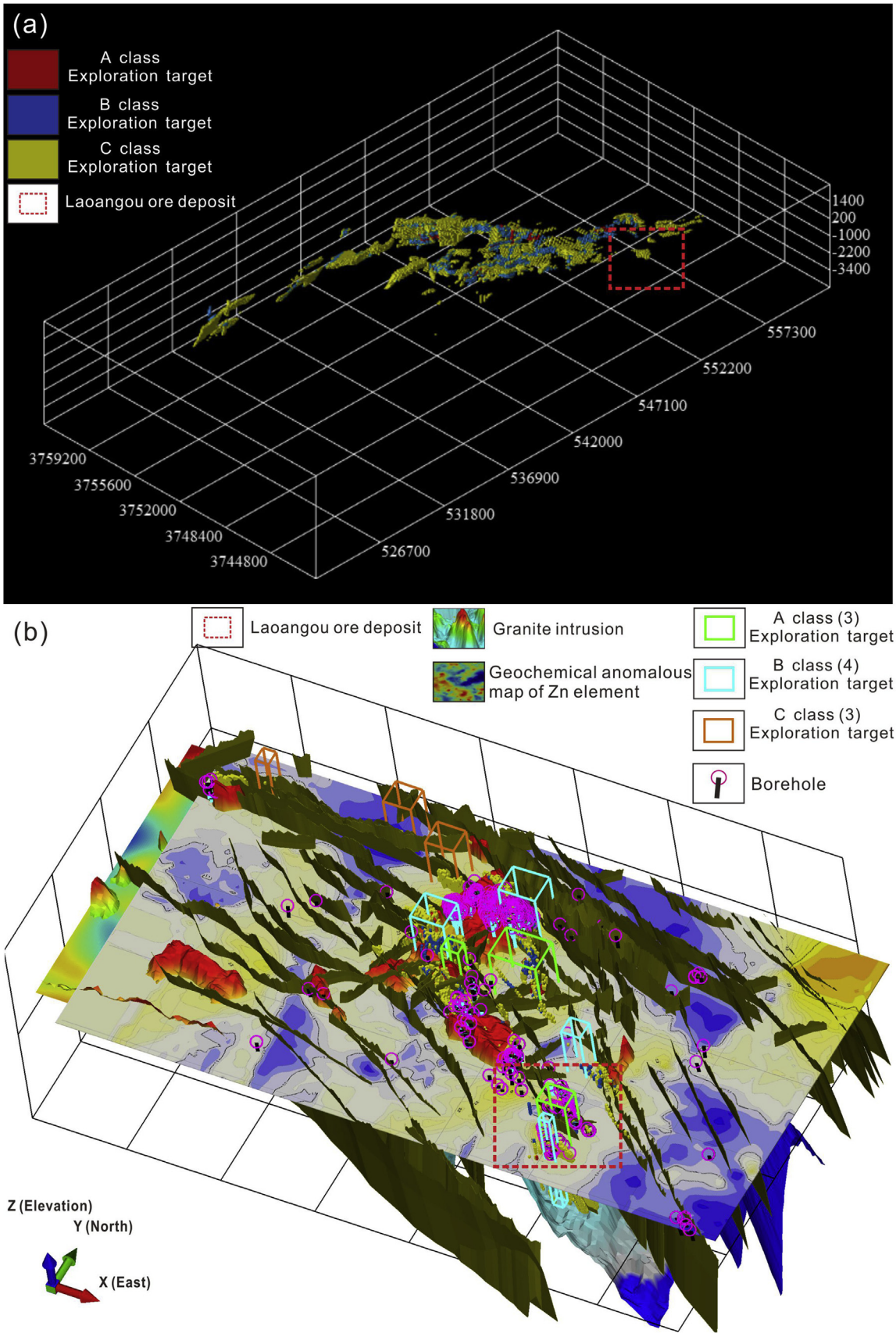


**Fig. 18.** 3D metallogenic model for Pb-Zn deposits in the LOD. (a) Delineated three classes (A–C) of exploration targets, (b) Subdivided targets (A, 3; B, 4; and C, 3) based on the three classes of exploration targets. (Modified after Yang, 2016).

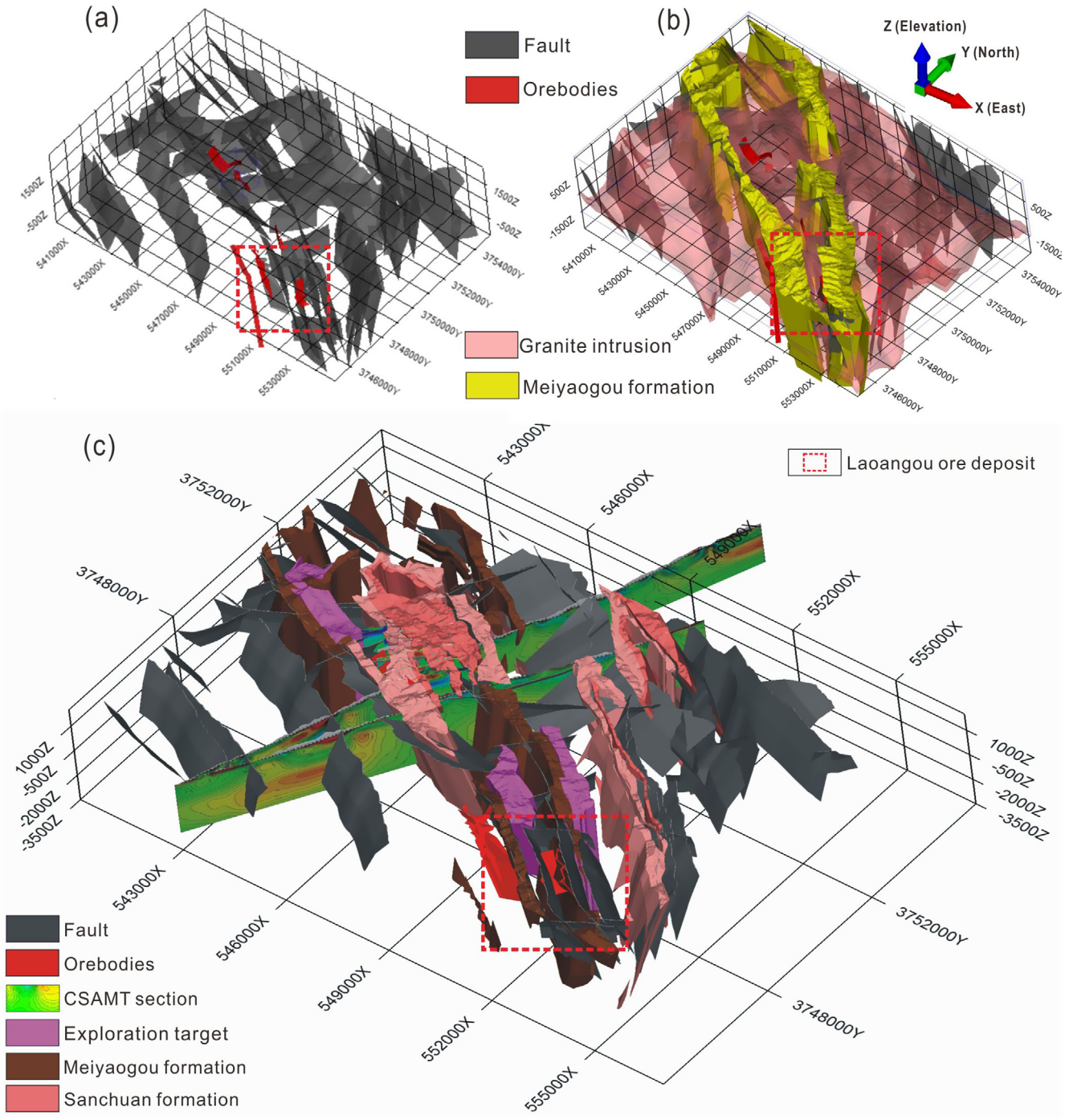


**Fig. 19.** 3D geological models of the CTD. (a) Superposition of faults and known orebodies, (b) Superposition of faults, known orebodies, strata and granite, and (c) 3D metallogenic models of exploration targets (Modified after Guo, 2015).

Li et al. (2016) conducted 3D prediction of Mo mineralization in the Nannihu ore field of LOD through the application of logistic regression and information entropy methods, further attesting to the validity of logistic regression and information entropy methods for metallogenic prediction in 3D space. They obtained three classes of exploration targets for guiding prospecting work from the 3D space. Guo (2015) carried out a deposit-scale 3D metallogenic prediction of Chitudian Pb-Zn deposit (CTD) for subsurface Pb-Zn-Ag targets in the LOD. Their study delineated three exploration targets based on the multiple datasets including geological data and section line profiles, geophysical data of CSAMT section, geochemical data of 1:50,000 scale stream sediment analysis, mineral analysis and remote sensing. An integration of these into 3D modeling resulted in the reconstruction of known orebodies based on the boreholes and section lines profiles (Fig. 19a–c). In Fig. 19, the CTD is typically controlled by NW-trending faults and hosted within the Sanchuan and Meiyaogou formations. However, the LAG is also located within the southeastern part of Chitudian Pb-Zn-Ag polymetallic metallogenic belt (Guang et al., 2013), and shows metallogenic setting and ore-controlling factors similar to those of CTD. Therefore, these exploration criteria used in this study is reasonable and logical.

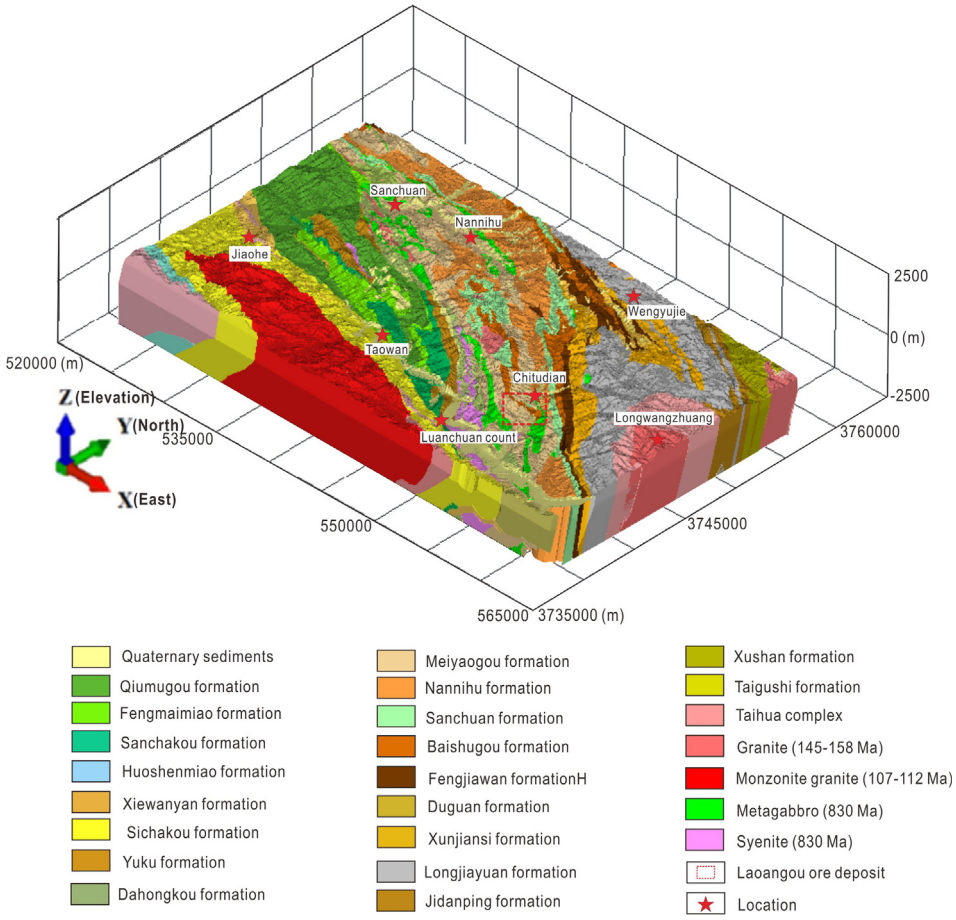


**Fig. 20.** 3D geological model of the lithological units in the LOD showing spatial distribution and location of the LAG (Modified after Wang et al., 2015).

Although the district-scale strata have been constructed by previous studies (Zhu, 2013; Wang et al., 2015) (Fig. 20), the results remain debated. These strata (Fig. 20) based district-scale 1:50,000 scale geological map as well as data from boreholes and section line profiles do not profile adequate details as compared with the results (Fig. 7a) obtained in our study based on the deposit-scale 1:10,000 scale geological map, and 1:1000 scale section line profiles and more boreholes. Similarly, the other exploration criteria are also more accurate in our work based on new data-set and their integration (Fig. 7). From results on CTD (Guo, 2015) (Fig. 19), these delineated exploration targets are mainly controlled by the NW-trending faults, and are particularly located within the zones of intersections between NW- and NE-trending faults, as well as hosted in the strata belonging to the Meiyaogou formation (Fig. 19a, c). As shown in the Fig. 13, the exploration targets identified in this study are similar to those from the CTD, and also consistent with the ore-controlling factors of CTD (Figs, 13 and 19). We therefore conclude that the exploration targets delineated in this study are reliable and can be used for exploration work in the 3D space.

## 8. Conclusions

(1) A comprehensive deposit-scale prediction model was constructed for extracting spatial features which represent exploration criteria from geological information in the LAG.
(2) The methods of ordinary WofE, weighted WofE, boost WofE, logistic regression and information entropy were used to integrate and extract these spatial features for exploration targeting, and the C–V fractal method is used for separating the prospect areas from background and further classifying the prediction results.
(3) Three levels of prospecting targets are delineated clearly. Among these, the first level targets are mainly distributed in the periphery of known orebodies (M2, M3, II-3 and VI), which are also located in the ore-controlling strata and fault zones; the second level targets are located in the known ore district, which do not provide further guidelines for prospecting, although they confirm that the prediction result is reliable; the third level targets, which are mainly located at the zone of contact between the ore-controlling strata and metagabbro, represent a new target exploration zone in the LAG.

## Acknowledgments

We are grateful to the Associate Editor Dr. Ignacio González-Álvarez and two anonymous reviewers for their constructive comments and suggestions which improved an earlier version of this paper. Fan Yang thanks Xuhuang Zhang, Junjun Li, Hui Yun and Jiangwei Han for kindly help in the field work, and his colleagues Botao Wen, Qidi Han, Shuai Zhang, Fei Xue, Wenjuan Jia and Zhiwei Shen for their communication during the 3D geological modeling. This work forms part of the PhD research of Fan Yang at the China University of Geosciences, Beijing. This research was jointly supported by the National Natural Science Foundation

of China (Grant No. 41572318) and the National Key Research Projects (Grant No. 2016YFC0600100; Grant No. 2016YFC0600500).

## References


Afzal, P., Fadakar, A.Y., Khakzad, A., Moarefvand, P., Rashidnejad, O.N., 2011. Delineation of mineralization zones in porphyry Cu deposits by fractal concentration–volume modelling. J. Geochem. Explor. 18, 220–232.

Agterberg, F.P., 1989. Systematic approach to dealing with uncertainty of geosciences information in mineral exploration. In: Proceedings of the 21st APCOM Symposium, Las Vegas, USA, Chapter, 18, pp. 165–178.

Agterberg, F.P., 1992. Combining indicator patterns in weights of evidence modeling for resource evaluation. Nonrenew. Resour. 1 (1), 39–50.

Agterberg, F.P., 2011. A modified weights-of-evidence method for regional mineral resource estimation. Nat. Resour. Res. 20 (2), 95–101.

Agterberg, F.P., Bonham-Carter, G.F., Wright, D.F., 1990. Statistical pattern integration for mineral exploration. In: Gaal, G., Merriam, D.F. (Eds.), Computer Applications in Resource Estimation: Predictions and Assessment for Metalsand Petroleum. Pergamon, Oxford, pp. 1–21.

Akgun, A., 2012. A comparison of landslide susceptibility maps produced by logistic regression, multi-criteria decision, and likelihood ratio methods: a case study at Izmir, Turkey. Landslides 9 (1), 93–106.

Ayalew, L., Yamagishi, H., 2005. The application of GIS-based logistic regression for landslide susceptibility mapping in the Kakuda-Yahiko Mountains, Central Japan. Geomorphology 65, 15–31.

Bao, Z.W., Zeng, Q.S., Zhao, T.P., Yuan, Z.L., 2009. Geochemistry and petrogenesis of the ore related Nannihu and Shangfanggou granite porphyries from East Qinling belt and their constrains on the molybdenum mineralization. Acta Petrol. Sin. 25, 2523–2536 (in Chinese with English abstract).

Bao, Z.W., Wang, C.Y., Zhao, T.P., Li, C.J., Gao, X.Y., 2014. Petrogenesis of the Mesozoic granites and Mo mineralization of the Luanchuan ore field in the East Qinling Mo mineralization belt, Central China. Ore Geol. Rev. 57, 132–153.

Ben-Naim, A., 2008. A Farewell to Entropy: Statistical Thermodynamics Based on Information. World Scientific Publishing Co., Pte. Ltd, Singapore, pp. 1–383.

Bonham-Carter, G.F., 1994. Geographic Information Systems for Geoscientists: Modelling with GIS. Computer Methods in the Geosciences. Pergamon, New York, pp. 1–414.

Bonham-Carter, G.F., Agterberg, F.P., Wright, D.F., 1988. Integration of geological datasets for gold exploration in Nova Scotia. Digital Geol. Geogr. Inf. Syst., 15–23

Bonham-Carter, G. F., Agterberg, F. P., Wright, D. F., 1989. Weights of evidence modelling: A new approach to mapping mineral potential. In: Agterberg, F.P., et al. (Eds.). Statistical Applications in the Earth Sciences. Geology Survey of Canada, Paper 89–9: 171–183.

Cao, H.W., Zhang, S.T., Santosh, M., Zheng, L., Tang, L., Li, D., Zhang, X.H., Zhang, Y.H., 2015. The Luanchuan Mo–W–Pb–Zn–Ag magmatic–hydrothermal system in the East Qinling metallogenic belt, China: constrains on metallogenesis from C-H–O–S–Pb isotope compositions and Rb–Sr isochron ages. J. Asian Earth Sci. 111, 751–780.

Carranza, E.J.M., 2009. Objective selection of suitable unit cell size in data-driven modeling of mineral prospectivity. Comput. Geosci. 35, 2032–2046.

Carranza, E.J.M., Hale, M., 2001. Logistic regression for geologically constrained mapping of gold potential, Baguio district, Philippines. Explor. Min. Geol. 10 (3), 165–175.

Carranza, E.J.M., Sadeghi, M., 2010. Predictive mapping of prospectivity and quantitative estimation of undiscovered VMS deposits in Skellefte district (Sweden). Ore Geol. Rev. 38, 219–241.

Chen, Y.J., Santosh, M., 2014. Triassic tectonics and mineral systems in the Qinling orogen, central China. Geol. J. 49, 338–358.

Cheng, Q.M., 2012. Application of a newly developed boost weights of evidence model (Boost WofE) for mineral resources quantitative assessments. J. Jilin Univ. Earth Sci. 42 (6), 1976–1984.

Cheng, Q.M., 2015. Boost WofE: a new sequential weights of evidence model reducing the effect of conditional dependency. Math. Geosci. 47 (5), 591–621.

Cheng, Q.M., Agterberg, F.P., 1999. Fuzzy weights of evidence method and its application in mineral potential mapping. Nat. Resour. Res. 8 (1), 27–35.

Cheng, Q.M., Agterberg, F.P., Ballantyne, S.B., 1994. The separation of geochemical anomalies from background by fractal methods. J. Geochem. Explor. 51 (2), 109–130.

Chung, C.F., Agterberg, F.P., 1980. Regression models for estimating mineral resources from geological map data. Math. Geol. 12 (5), 473–488.

Dai, F.C., Lee, C.F., 2002. Landslide characteristics and slope instability modeling using GIS, Lantau Island, Hong Kong. Geomorphology 42, 213–228.

Deng, Z., Liu, S., Zhang, W., Hu, F., Li, Q., 2016. Petrogenesis of the Guangtoushan granitoid suite, central China: implications for Early Mesozoic geodynamic evolution of the Qinling Orogenic Belt. Gondwana Res. 30, 112–131.

Dong, Y., Santosh, M., 2016. Tectonic architecture and multiple orogeny of the Qinling orogenic belt, Central China. Gondwana Res. 29, 1–40.

Dong, Y.P., Zhang, G.W., Neubauer, F., Liu, X.M., Genser, J., Hauzenberger, C., 2011. Tectonic evolution of the Qinling orogen, China: review and synthesis. J. Asian Earth Sci. 41, 213–237.

Duan, S.G., Xue, C.J., Liu, G.Y., Yan, C.H., Feng, Q.W., Song, Y.W., Chu, J.J., 2010. Geology and sulfur isotope geochemistry of lead-zinc deposits in Luanchuan district, Henan Province, China. Earth Sci. Front. 17, 375–384.

Ford, A., Miller, J.M., Mol, A.G., 2016. A comparative analysis of weights of evidence, evidential belief functions, and fuzzy logic for mineral potential mapping using incomplete data at the scale of investigation. Nat. Resour. Res. 25 (1), 19–33.

Guang, H., Wu, E.B., Yang, J.T., Fang, H., Li, W.L., 2013. The prospecting report of Production in the Laoangou Pb-Zn-Ag polymetallic Deposit, Henan Province, China. Henan Institute of Geological Prospecting of Zhonghua Gological Administration Press, pp. 1–63 (in Chinese).

Guo, N.N., 2015. Metallogenic Prediction based on 3-D Geological Modeling System and Remote Sensing Technologies – A Case Study of Chitudian Lead-Zinc ore district, Luanchuan County, Henan Province, China. University of Geosciences Press, Beijing, pp. 1–98 (in Chinese with English abstract).

Guo, J.H., Chen, F.K., Zhang, X.M., Siebel, W., Zhai, M.G., 2005. Evolution of syn-to post-collisional magmatism from north Sulu UHP belt, eastern China: zircon U-Pb geo-chronology. Acta Petrol. Sin. 4, 1281–1301 (in Chinese with English abstract).

Hamedani, M.L., Plimer, I.R., Xu, C., 2012. Orebody modelling for exploration: the Western mineralisation, Broken Hill, NSW. Nat. Resour. Res. 21 (3), 325–345.

Harris, D., Pan, G., 1999. Mineral favorability mapping: a comparison of artificial neural networks, logistic regression, and discriminant analysis. Nat. Resour. Res. 8 (2), 93–109.

He, J., Yao, S., Zhang, Z., You, G., 2013. Complexity and productivity differentiation models of metallogenic indicator elements in rocks and supergene media around Daijiazhuang Pb–Zn deposit in Dangchang County, Gansu Province. Nat. Resour. Res. 22, 19–36.

Hosmer, D.W., Lemeshow, S., 2004. Applied Logistic Regression. John Wiley & Sons, United States.

Hu, F., Liu, S., Santosh, M., Deng, Z., Wang, W., Zhang, W., Yan, M., 2016. Chronology and tectonic implications of Neoproterozoic blocks in the south Qinling Orogenic Belt, Central China. Gondwana Res. 30, 24–47.

Jiang, Y., Jin, G., Liao, S., 2010. Geochemical and Sr-Nd-Hf isotopic constraints on the origin of Late Triassic granitoids from the Qinling orogen, central China: implications for a continental arc to continent–continent collision. Lithos 117, 183–197.

Kaufmann, O., Martin, T., 2008. 3D geological modelling from boreholes, cross-sections and geological maps, application over former natural gas storages in coal mines. Comput. Geosci. 34, 278–290.

Kavzoglu, T., Sahin, E.K., Colkesen, I., 2014. Landslide susceptibility mapping using GIS-based multi-criteria decision analysis, support vector machines, and logistic regression. Landslides 11 (3), 425–439.

Li, Y.F., Mao, J.W., Guo, B.J., Shao, Y.J., Fei, H.C., Hu, H.B., 2004. Re-Os Dating of Molybdenite from the Nannihu Mo (-W) Orefield in the East Qinling and Its Geodynamic Significance. Acta Geol. Sin. (English Edition) 78, 463–470.

Li, Y., Mao, J., Hu, H., Guo, B., Bai, F., 2005. Geology, distribution, types and tectonic settings of Mesozoic molybdenum deposits in East Qinling area. Min. Depos. 24 (3), 292–304.

Li, N., Chen, Y.J., Zhang, H., Zhao, T.P., Deng, X.H., Wang, Y., Ni, Z.Y., 2007. Molybdenum deposits in East Qinling. Earth Sci. Front. 14, 186–198 (in Chinese with English abstract).

Li, D., Zhang, S.T., Yan, C.H., Wang, G.W., Song, Y.W., Ma, Z.B., Han, J.W., 2012. Late Mesozoic time constraints on tectonic changes of the Luanchuan Mo belt, East Qinling orogen, Central China. J. Geodyn. 61, 94–104.

Li, S.R., Santosh, M., Zhang, H.F., Shen, J.F., Dong, G.C., Wang, J.Z., Zhang, J.Q., 2013. Inhomogeneous lithospheric thinning in the central North China Craton: zircon U-Pb and S-He-Ar isotopic record from magmatism and metallogeny in the Taihang Mountains. Gondwana Res. 23, 141–160.

Li, X.H., Yuan, F., Zhang, M.M., Jia, C., Jowitt, S.M., Ord, A., Zheng, T.K., Hu, X.Y., Li, Y., 2015a. Three-dimensional mineral prospectivity modeling for targeting of concealed mineralization within the Zhonggu iron orefield, Ningwu Basin, China. Ore Geol. Rev. 71, 633–654.

Li, D., Han, J.W., Zhang, S.T., Yan, C.H., Cao, H.W., Song, Y.W., 2015b. Temporal evolution of granitic magmas in the Luanchuan metallogenic belt, east Qinling Orogen, central China: implications for Mo metallogenesis. J. Asian Earth Sci. 111, 663–680.

Li, N., Chen, Y.J., Santosh, M., Pirajno, F., 2015c. Compositional polarity of Triassic granitoids in the Qinling Orogen, China: implication for termination of the northernmost paleo-Tethys. Gondwana Res. 27 (1), 244–257.

Li, R.X., Wang, G.W., Carranza, E.J.M., 2016. GeoCube: a 3D mineral resources quantitative prediction and assessment system. Comput. Geosci. 89, 161–173.

Liu, G.Y., 2007. The Pb-Zn-Ag Metallogeny and Prospecting Target in the South Marge of North China Craton. China University of Geoscience, Beijing, pp. 22–38.

Liu, Z.H., Wang, S.Y., Zhang, L., 2004. The Jurassic magmatism of intracratonic orogenin the Southern margin of the North China craton. Geol. Survey Res. 27 (1), 35–42.

Luz, F., Mateus, A., Matos, J.X., Gonçalves, M.A., 2014. Cu- and Zn-soil anomalies in the NEBorder of the South Portuguese Zone (Iberian Variscides, Portugal) identified bymultifractal and geostatistical analyses. Nat. Resour. Res. 23, 195–215.

Mao, J.W., Xie, G.Q., Zhang, Z.H., Li, X.F., Wang, Y.T., Zhang, C.Q., Li, Y.F., 2005. Mesozoic large-scale metallogenic pulses in North China and corresponding geodynamic settings. Acta Petrol. Sin. 21 (1), 169–188 (in Chinese with English abstract).

Mao, J.W., Xie, G.Q., Bierlein, F., Qü, W.J., Du, A.D., Ye, H.S., Pirajno, F., Li, H.M., Guo, B. J., Li, Y.F., 2008. Tectonic implications from Re-Os dating of Mesozoic molybdenum deposits in the East Qinling-Dabie orogenic belt. Geochim. Cosmochim. Acta 72 (18), 4607–4626.

Mao, J.W., Xie, G.Q., Pirajno, F., Ye, H.S., Wang, Y.B., Li, Y.F., Xiang, J.F., Zhao, H.J., 2010. Late Jurassic-Early Cretaceous granitoid magmatism in Eastern Qinling, central-eastern China: SHRIMP zircon U-Pb ages and tectonic implications. Aust. J. Earth Sci. 57 (1), 51–78.
Mao, J.W., Pirajno, F., Xiang, J.F., Gao, J.J., Ye, H.S., Li, Y.F., Guo, B.J., 2011a. Mesozoic molybdenum deposits in the East Qinling-Dabie Orogenic belt: characteristics and tectonic settings. Ore Geol. Rev. 43, 264–293.
Mao, X., Zou, Y., Cheng, J., Lai, J., Peng, S., 2011b. Three-Dimensional Visual Prediction of Concealed Orebodies. Central South University Press, Changsha.
Martelet, G., Calcagno, P., Gumiaux, C., Truffert, C., Bitri, A., Gapais, D., Brun, J.P., 2004. Integrated 3D geophysical and geological modelling of the Hercynian Suture Zone in the Champtoceaux area (South Brittany, France). Tectonophysics 382 (1), 117–128.
Mejía-Herrera, P., Royer, J.J., Caumon, G., Cheilletz, A., 2015. Curvature attribute from surface-restoration as predictor variable in Kupferschiefer copper potentials. Nat. Resour. Res. 24 (3), 275–290.
Menard, S., 2001. Applied Logistic Regression Analysis. Sage Publication, Thousand Oaks, California, pp. 1–119.
Meng, Q.R., Zhang, G.W., 2000. Geologic framework and tectonic evolution of the Qinlingorogen, Central China. Tectonophysics 323, 183–196.
Mohammady, M., Pourghasemi, H.R., Pradhan, B., 2012. Landslide susceptibility mapping at Golestan Province, Iran: a comparison between frequency ratio, Dempster-Shafer, and weights-of-evidence models. J. Asian Earth Sci. 61, 221–236.
Nielsen, S.H., Cunningham, F., Hay, R., Partington, G., Stokes, M., 2015. 3D prospectivity modelling of orogenic gold in the Marymia Inlier, Western Australia. Ore Geol. Rev. 71, 578–591.
Ozdemir, A., Altural, T., 2013. A comparative study of frequency ratio, weights of evidence and logistic regression methods for landslide susceptibility mapping: Sultan Mountains, SW Turkey. J. Asian Earth Sci. 64, 180–197.
Pirajno, F., 2013. Orogenic Belts: South China, Central China and Qinling-Dabie, Hinggan. The Geology and Tectonic Settings of China's Mineral Deposits. Springer, Berlin, pp. 249–380.
Porwal, A., González-Álvarez, I., Markwitz, V., McCuaig, T.C., Mamuse, A., 2010. Weights-of-evidence and logistic regression modeling of magmatic nickel sulfide prospectivity in the Yilgarn Craton, Western Australia. Ore Geol. Rev. 38 (2010), 184–196.
Pouliot, J., Bedard, K., Kirkwood, D., Lachance, B., 2008. Reasoning about geological space: coupling 3D Geo Models and topological queries as an aid to spatial data selection. Comput. Geosci. 34, 529–541.
Ratschbacher, L., Hacker, B.R., Calvert, A., Webb, L.E., Grimmer, J.C., McWilliams, M. O., Ireland, T., Dong, S.W., Hu, J.M., 2003. Tectonics of the Qinling (Central China): tectono stratigraphy, geochronology, and deformation history. Tectonophysics 366 (1), 1–53.
Santosh, M., 2013. Evolution of continents, cratons and supercontinents: building the habitable Earth. Curr. Sci. (Bangalore) 104 (7), 871–879.
Schaeben, H., 2014. Targeting: logistic regression, special cases and extensions. ISPRS Int. J. Geo-Inf. 3 (4), 1387–1411.
Shahriari, H., Ranjbar, H., Honarmand, M., 2013. Image segmentation for hydrothermalalteration mapping using PCA and concentration–area fractal model. Nat. Resour. Res. 22, 191–206.
Shannon, E.C., 1948. A mathematical theory of communication. Bell Syst. Tech. J. 27, 379–423.
Shao, Y.L., Zheng, A.L., He, Y.B., Xiao, K.Y., 2011. 3D geological modeling and its application under complex geological conditions. Proc. Eng. 12, 41–46.
Singer, D.A., 2008. Mineral deposit densities for estimating mineral resources. Math. Geosci. 40, 33–46.
Sun, W.D., Li, S.G., Sun, Y., Zhang, G.W., Li, Q.L., 2002. Mid-paleozoic collision in the north Qinling: Sm–Nd, Rb–Sr and $^{40}Ar/^{39}Ar$ ages and their tectonic implications. J. Asian Earth Sci. 21, 69–76.
Tang, L., Santosh, M., Dong, Y.P., 2015. Tectonic evolution of a complex orogenic system: evidence from the northern Qinling belt, central China. J. Asian Earth Sci. 113, 544–559.
Tang, L., Santosh, M., Dong, Y.P., Tsunogae, T., Zhang, S.T., Cao, H.W., 2016. Early Paleozoic tectonic evolution of the North Qinling orogenic belt: evidence from geochemistry, phase equilibrium modeling and geochronology of metamorphosed mafic rocks from the Songshugou ophiolite. Gondwana Res. 30, 48–64.
Vysokoostrovskaya, E.B., Zelenetsky, D.S., 1968. On quantitative evaluation of the prospects of a territory when searching for ore mineral deposits. Sov. Geol. 8, 58–71.
Wang, G.W., Huang, L., 2012. 3D geological modeling for mineral resource assessment of the Tongshan Cu deposit, Heilongjiang Province, China. Geosci. Front. 3 (4), 483–491.
Wang, X.L., Jiang, S.Y., Dai, B.Z., Griffin, W.L., Dai, M.N., Yang, Y.H., 2011a. Age, geochemistry and tectonic setting of the Neoproterozoic (ca 830 Ma) gabbroson the southern margin of the North China Craton. Precambr. Res. 190, 35–47.
Wang, G.W., Zhang, S.T., Yan, C.H., Song, Y.W., Sun, Y., Li, D., Xu, F.M., 2011b. Mineral potential targeting and resource assessment based on 3D geological modeling in Luanchuan region, China. Comput. Geosci. 37, 1976–1988.
Wang, G., Zhu, Y., Zhang, S., Yan, C., Song, Y., Ma, Z., Hong, D., Chen, T., 2012a. 3D geological modeling based on gravitational and magnetic data inversion in the Luanchuan ore region, Henan Province, China. J. Appl. Geophys. 80, 1–11.
Wang, G.W., Zhang, S.T., Yan, C.H., Xu, G.Y., Ma, M., Li, K., Feng, Y., 2012b. Application of the multifractal singular value decomposition for delineating geophysical anomalies associated with molybdenum occurrences in the Luanchuan ore field (China). J. Appl. Geophys. 86, 109–119.
Wang, C.M., He, X.U., Yan, C.H., Lü, W.D., Sun, W.Z., 2013. Ore geology, and H, O, S, Pb, Ar isotopic constraints on the genesis of the Lengshuibeigou Pb–Zn–Ag deposit, China. Geosci. J. 17, 197–210.
Wang, G.W., Li, R.X., Carranza, E.J.M., Zhang, S.T., Yan, C.H., Zhu, Y.Y., Qu, J.N., Hong, D.M., Song, Y.W., Han, J.W., Ma, Z.B., Zhang, H., Yang, F., 2015. 3D geological modeling for prediction of subsurface Mo targets in the Luanchuan district, China. Ore Geol. Rev. 71, 592–610.
Wang, G.W., Ma, Z.B., Li, R.X., Song, Y.W., Qu, J.N., Zhang, S.T., Yan, C.H., Han, J.W., 2017. Integration of multi-source and multi-scale datasets for 3D structural modeling for subsurface exploration targeting, Luanchuan Mo-polymetallic district, China. J. Appl. Geophys. 139, 269–290.
Wellmann, J.F., Regenauer-Lieb, K., 2012. Uncertainties have a meaning: Information entropy as a quality measure for 3-D geological models. Tectonophysics 526, 207–216.
Wu, Y.B., Zheng, Y.F., 2013. Tectonic evolution of a composite collision orogen: an overview on the Qinling-Tongbai-Hong'an-Dabie-Sulu orogenic belt in central China. Gondwana Res. 23, 1402–1428.
Xiang, J.F., Pei, R.F., Ye, H.S., Wang, C.Y., Tian, Z.H., 2012. Source and evolution of the ore-forming fluid in the Nannihu-Sandaozhuang Mo (W) deposit: constraints from C-H-O stable isotope data. Geol. China 39 (6), 1778–1789 (in Chinese with English abstract).
Xiao, B., Li, Q.G., He, S.Y., Chen, X., Liu, S.W., Wang, Z.Q., Xu, X.Y., Chen, J.L., 2017. Contrasting geochemical signatures between Upper Triassic Mo-hosting and barren granitoids in the central segment of the South Qinling orogenic belt, central China: implications for Mo exploration. Ore Geol. Rev. 81, 518–534.
Xue, F., Wang, G., Santosh, M., Yang, F., Shen, Z., Kong, L., Guo, N., Zhang, X., 2017. Geochemistry and geochronology of ore-bearing and barren intrusions in the Luanchuan ore fields of East Qinling metallogenic belt, China: diverse tectonic evolution and implications for mineral exploration. J. Asian Earth Sci. http://dx.doi.org/10.1016/j.jseaes.2017.04.027.
Yang, F., 2016. 3D Geological Modeling and Metallogenic Prediction in Luanchuan Pb-Zn Ore Concentration District, Henan Province, China. China University of Geosciences Press, Beijing, pp. 1–86 (in Chinese with English abstract).
Yang, Y., Wang, X.X., Ke, C.H., Li, J.B., 2012. Zircon U-Pb age, geochemistry and Hf isotopic compositions of Shibaogou granitoid pluton in the Nannihu ore district, Western Henan Province. Geol. China 39 (6), 1525–1542 (in Chinese with English abstract).
Yang, Y., Chen, Y.J., Zhang, J., Zhang, C., 2013. Ore geology, fluid inclusions and four-stage hydrothermal mineralization of the Shangfanggou giant Mo-Fe deposit in Eastern Qinling, Central China. Ore Geol. Rev. 55, 146–161.
Yang, C.Y., Ye, H.S., Xiang, J.F., Chen, X.D., Xing, B., Li, L., Wang, S., 2015. Rb-Sr isochron age of sulfide from Luotuoshan polymetallic deposit in West Henan Province and its geological significance. The 15th annual seminar abstract of Chinese Society for Mineralogy, Petrology and Geochemistry, 3 (in Chinese).
Yang, F., Wang, G.W., Cao, H.W., Li, R.X., Tang, L., Huang, Y.F., Zhang, H., Xue, F., Jia, W.J., Guo, N.N., 2016. Timing of formation of the Hongdonggou Pb-Zn-Ag polymetallic polymetallic ore deposit, Henan Province, China: evidence from Rb-Sr isotopic dating of sphalerites. Geosci. Front. http://dx.doi.org/10.1016/j.gsf.2016.06.001.
Yang, F., Santosh, M., Tsunogae, T., Tang, L., Teng, X., 2017. Multiple magmatism in an evolving suprasubduction zone mantle wedge: The case of the composite mafic-ultramafic complex of Gaositai, North China Craton. Lithos. http://dx.doi.org/10.1016/j.lithos.2017.05.004.
Yuan, F., Li, X.H., Zhang, M.M., Jowitt, S.M., Jia, C., Zheng, T.K., Zhou, T.F., 2014. Three-dimensional weights of evidence-based prospectivity modeling: a case study of the Baixiangshan mining area, Ningwu Basin, Middle and Lower Yangtze Metallogenic Belt, China. J. Geochem. Explor. 145, 82–97.
Zhai, M.G., Santosh, M., 2013. Metallogeny of the North China Craton: link with secular changes in the evolving Earth. Gondwana Res. 24, 275–297.
Zhang, Y.H., 2014. Late-Mesozoic Tectonic-magma Evolution and its Relationship with Mineralization in Luanchuan County. China University of Geosciences (Beijing), Beijing, pp. 1–79 (in Chinese with English abstract).
Zhang, Q., Qian, Q., Wang, E.C., Wang, Y., Zhao, T.P., Hao, J., 2001. Existence of the East China Plateau in the mid-late Yanshan period: implications from adakites. Sci. Geol. Sin. 36, 248–255 (in Chinese with English abstract).
Zhang, D., Agterberg, F., Cheng, Q., Zuo, R., 2014. A comparison of modified fuzzy weights of evidence, fuzzy weights of evidence, and logistic regression for mapping mineral prospectivity. Math. Geosci. 46 (7), 869–885.
Zhu, Y.Y., 2013. 3D Geological Modeling and Metallogenic Prediction in Luanchuan Polymetallic District, Henan Province, China. China University of Geosciences Press, Beijing, pp. 1–50.
Zhu, L.M., Zhang, G.W., Guo, B., Lee, B., 2009. He-Ar isotopic system of fluid inclusions in pyrite from the molybdenum deposits in south margin of North China Block and its trace to metallogenetic and geodynamic background. Chin. Sci. Bull. 54, 2479–2492.